J. Fluid Mech. (2015), *vol.* 769, *pp.* 654–686. © Cambridge University Press 2015
doi:10.1017/jfm.2015.122

Scaling of second- and higher-order structure functions in turbulent boundary layers

C. M. de Silva[1,†], I. Marusic[1], J. D. Woodcock[1] and C. Meneveau[2]

[1]Department of Mechanical Engineering, University of Melbourne, Australia

[2]Department of Mechanical Engineering, Johns Hopkins University, 3400 N. Charles Street, Baltimore, MD 21218, USA

(Received 17 December 2014; revised 8 February 2015; accepted 19 February 2015; first published online 30 March 2015)

The statistical properties of wall turbulence in the logarithmic region are investigated using structure functions of the streamwise velocity. To this end, datasets that span several orders of magnitude of Reynolds numbers are used, up to $Re_\tau = O(10^6)$, providing uniquely large scale separations for scrutinising previously proposed scaling laws. For the second-order structure functions strong support is found simultaneously for power-law scalings in the Kolmogorov inertial subrange and for logarithmic scaling at larger scales within the inertial range ($z < r \ll \delta$, where z is the distance from the wall, r the scale, and δ the boundary layer thickness). The observed scalings are shown to agree between the datasets, which include both temporal and spatial velocity signals and span from laboratory to atmospheric flows, showing a degree of universality in the results presented. An examination of higher even-order structure functions also shows support for logarithmic scaling behaviour for $z < r \ll \delta$, provided that the Reynolds number is sufficiently high. These findings are interpreted by generalising the work of Meneveau & Marusic (*J. Fluid Mech.*, vol. 719, 2013) and introducing bridging relations between higher-order moments of velocity fluctuations and structure functions. Further, a physical model based on the attached-eddy hypothesis is utilised to derive various properties of the structure functions for the energy-containing scales of the logarithmic region. The descriptions derived from the model are shown to be supported by the experimental data.

Key words: turbulence theory, turbulent boundary layers, turbulent flows

1. Introduction

High-Reynolds-number wall turbulence is a commonly observed phenomenon and plays a central role in many engineering, environmental and geophysical flows. A robust feature of these flows, and one that is relied upon extensively for modelling purposes, is the logarithmic region (Smits, McKeon & Marusic 2011; Jiménez 2012), where the logarithmic law of the wall applies for the streamwise mean velocity. More recently, however, there is growing evidence also for logarithmic behaviour in the variance of both the streamwise (Hultmark 2012; Marusic *et al.* 2013) and spanwise (Pirozzoli & Bernardini 2013; Sillero, Jiménez & Moser 2013; Talluru *et al.* 2014) velocity fluctuations, and these observations are as predicted by the

† Email address for correspondence: desilvac@unimelb.edu.au

attached-eddy hypothesis of Townsend (1976). Townsend's hypothesis has become the basis of a physical model for wall turbulence (Perry & Chong 1982; Perry, Henbest & Chong 1986; Perry & Marusic 1995; Marusic 2001), where the flow field in the logarithmic region is modelled by a hierarchy of spatially self-similar eddies, whose dimensions scale with their distance from the wall. Recently, Woodcock & Marusic (2015) revisited the attached-eddy model and applied an extended form of Campbell's theorem to derive expressions for the functional forms of all moments of the velocities, including cross-correlations. In this way, they were able to verify the earlier results of Townsend (1976) and Perry & Chong (1982) for the mean flow and the variances, and the recent findings of Meneveau & Marusic (2013) that all even-ordered moments of the streamwise velocity also exhibit a logarithmic dependence on the distance from the wall, once the Reynolds number is sufficiently high.

The distribution of energy across spatial scales prevalent in the logarithmic region is also of particular interest. This aspect has been studied extensively using both the one-dimensional power spectrum and the second-order structure function for the streamwise velocity. The k^{-1} spectral law (where k represents the streamwise wavenumber) has been predicted in the one-dimensional power spectrum of the streamwise velocity, $\phi_{uu}(k)$, by various physical arguments (Högström, Hunt & Smedman 2002; Davidson & Krogstad 2009, and others) and has been directly linked by Perry *et al.* (1986) to the logarithmic formulation for the streamwise velocity variance by scaling arguments based on the attached-eddy hypothesis. While experimental support for a k^{-1} spectral law at sufficiently high Reynolds numbers has been reported by Nickels *et al.* (2005), in general definitive experimental evidence has been elusive (Morrison *et al.* 2004; Zhao & Smits 2007). Concurrently, increased support for a k^{-1} spectral law has also been presented from recent numerical work as higher Reynolds numbers become realisable in simulations (Pirozzoli & Bernardini 2013; Bernardini, Pirozzoli & Orlandi 2014; Lee & Moser 2015). Davidson, Nickels & Krogstad (2006*b*) considered this issue in detail and concluded that the one-dimensional spectrum of streamwise velocity is not the ideal parameter to investigate scaling behaviour in the logarithmic region, due to measurement aliasing and other challenges, and proposed that structure functions provided a diagnostic that could be interpreted more clearly. Further, structure functions computed at higher orders provide additional statistical information, which is not available in a spectral space that only describes second-order statistics.

Davidson *et al.* (2006*b*) showed that the analogous counterpart to the k^{-1} spectral law was a $\ln(r/z)$ law for the second-order structure function, where r is the spatial separation in the streamwise direction and z is the distance from the wall. Experimental evidence for a $\ln(r/z)$ law for the second-order structure function was presented by Davidson and coworkers (Davidson, Krogstad & Nickels 2006*a*; Davidson *et al.* 2006*b*; Davidson & Krogstad 2009). Their work shows that the $\ln(r/z)$ law extends from the largest length scales that bound the Kolmogorov inertial subrange from above, $r \approx z$ (see Tennekes & Lumley 1972), up to the large scale contribution range associated with eddies that scale in the order of δ (boundary layer thickness). More recent studies using structure functions have shown universality in scaling behaviour using data from both smooth and rough boundary layers (Davidson & Krogstad 2014), closely following the expected behaviour based on models and outer layer similarity described in Perry & Li (1990) and Schultz & Flack (2005).

At sufficiently high Reynolds numbers, one also expects an inertial subrange residing at scales that are larger than the dissipative range but smaller than those

associated with the k^{-1} spectral or $\ln(r/z)$ law. In this range, turbulence is expected to be locally isotropic, as described by Kolmogorov (1941), with $k^{-5/3}$ and $(r/z)^{2/3}$ scalings for the spectrum and second-order structure function respectively. The notion of universality provided great impetus for the study of small scales, which has led to a wide array of studies (reviewed by Sreenivasan & Antonia 1997) that extended the seminal work of Kolmogorov (1941). Of particular interest are the scaling exponents of the power-law behaviour observed in structure functions within the inertial subrange (Anselmet *et al.* 1984; Meneveau & Sreenivasan 1987; She & Leveque 1994). Subsequently, the influence of intermittency in small-scale turbulence has also gained attention in a range of studies, including wall-bounded turbulence (Benzi *et al.* 1999; Toschi *et al.* 1999; Poggi, Porporato & Ridolfi 2003; Jacob *et al.* 2004, and others) and homogeneous shear flows (Gualtieri *et al.* 2002; Casciola *et al.* 2003, 2005), where focus is placed on improving intermittency models. Several of these studies have shown the benefits of using the $SO(3)$ decomposition to isolate isotropic and anisotropic effects to observe scaling behaviour in inhomogeneous and anisotropic turbulent flows. However, this approach requires spatial information and is more readily applicable to numerical simulation databases (Arad *et al.* 1999).

Among the many studies that have considered structure functions in turbulent shear flows one notable result is the presence of a transition length scale (L_s) (Hinze 1975; Toschi *et al.* 1999). At scales larger than L_s shear is considered to be important, whereas at smaller scales shear is relatively unimportant. Consequently, one expects the structure function to scale differently on either side of L_s.

The results of Davidson and coworkers (Davidson *et al.* 2006*a*,*b*; Davidson & Krogstad 2009) provide an interesting connection between the inertial subrange and the scales above $r/z \sim 1$ for the second-order structure functions. Insights relating exponents and prefactors in the respective scaling laws were obtained by properly matching the two behaviours at scales when $r/z \sim 1$.

Here, we consider the abovementioned scaling behaviours using five experimental datasets in boundary layer flows that span several decades of Reynolds numbers (Re). This significantly extends the range of scales available for the analysis and enables us to observe scaling laws unambiguously. Moreover, we also consider structure functions of higher orders. Using a uniquely large range of Re, the results provide experimental evidence that scaling laws for higher-order moments also lead to interesting connections between the two ranges that must meet at $r/z \sim 1$. The experimental results are complemented with analysis that aims at connecting the results with those obtained in Meneveau & Marusic (2013). Furthermore, we explore the predictive power of the attached-eddy hypothesis in studying the high-order structure functions in the $\ln(r/z)$ range of r space.

The paper is organised as follows. Section 2 provides a short summary of prior relevant results in scaling of second-order structure functions, higher-order moments of the velocity fluctuations and anomalous scaling (intermittency) in the inertial range. These prior results provide motivation for measurements of the structure functions over a vast range of scales and distances to the wall. Section 3 provides a description of the experimental datasets used. The main results obtained from each dataset for second- and higher-order streamwise structure functions are presented in § 4. These results are then followed in § 5 by a discussion of possible bridging relations connecting the higher-order moments of structure functions to those of the velocity fluctuations, generalising the results of Meneveau & Marusic (2013). Then we show how the results in the $\ln(r/z)$ range are consistent with a physical model of the local large scales of the flow in § 5.2. There it is shown that the attached-eddy hypothesis may in fact be

used to compute high-order moments of the structure functions, leading to concrete connections between the observed parameters of the scaling laws and those of the assumed distributions of eddies in the hierarchy. Section 6 discusses the universality of the coefficients computed for the scaling laws described in §§ 2 and 5, followed by a discussion on modelling the behaviour of the streamwise structure function based on established results from the inertial subrange.

Throughout this paper, the coordinate system x, y and z refers to the streamwise, spanwise and wall-normal directions respectively. The corresponding instantaneous streamwise, spanwise and wall-normal velocity fluctuations are represented by u, v and w. Overbars and $\langle\,\rangle$ indicate averaged quantities, and superscript and subscript $+$ signs refer to normalisation by inner scales. For example, we use $l^+ = lU_\tau/\nu$ for length and $u^+ = u/U_\tau$ for velocity, where U_τ is the mean friction velocity and ν is the kinematic viscosity of the fluid.

2. Relevant details from prior works on structure functions and extensions

This section provides the relevant background on scaling laws for the streamwise structure functions in turbulent boundary layers. Here, we define the streamwise structure function following the common notation

$$\langle \Delta u^n(r)\rangle = \langle [u(\boldsymbol{x}+\boldsymbol{i}r) - u(\boldsymbol{x})]^n\rangle, \tag{2.1}$$

where r represents the spatial separation, n is a positive integer indicating the moment order and $\boldsymbol{i}$ is the unit vector in the streamwise direction. As summarised by Davidson *et al.* (2006*b*), the second-order structure functions in the logarithmic region of a turbulent boundary layer are postulated to have four regions. At the smallest length scales where $r \ll z$, Kolmogorov scaling is prevalent. At the other extreme $r \gg \delta$, $\langle \Delta u^2\rangle$ is independent of r and asymptotes to twice the streamwise turbulence intensity $2\langle u^2\rangle$. Here, we focus on the two regions in between. Nevertheless, a brief summary of the relevant scaling for each of the four regions follows.

2.1. *Structure functions at dissipative scales*

At the smallest scales (Kolmogorov scales), using a Taylor series expansion with the assumption of homogeneous isotropic turbulence at these scales (Frisch 1995) we expect a scaling behaviour of $\langle \Delta u^2\rangle$ according to

$$\langle \Delta u^2\rangle = \frac{\epsilon}{15\nu} r^2, \tag{2.2}$$

where ϵ denotes the dissipation rate. For the presented analysis we limit ourselves to the logarithmic region in wall-normal space of high Reynolds number turbulent boundary layers. Within this region, there is a near balance between the turbulent production ($\mathscr{P}$) and dissipation (ϵ) rates (Tennekes & Lumley 1972; Townsend 1976, and others). Thus,

$$\mathscr{P} \approx \epsilon \approx \frac{U_\tau^3}{\kappa z}, \tag{2.3}$$

where κ is von Kármán's constant. We note that Davidson *et al.* (2006*b*) have explored deviations from this equilibrium assumption at lower Re. In wall-bounded turbulence at wall-normal locations within the logarithmic region (2.2) simplifies to

$$\langle \Delta u_+^2\rangle = \frac{z^+}{15\kappa}\left(\frac{r}{z}\right)^2, \tag{2.4}$$

which holds at scales smaller than the Kolmogorov length, $0 < r \lesssim \eta = (\nu^3/\epsilon)^{1/4}$, i.e. $r/z \lesssim z_+^{-3/4}\kappa^{1/4}$. A Taylor series expansion also leads to integer scaling exponents for higher-order structure functions ($\langle \Delta u^n \rangle \sim r^n$) in the dissipative range (Nelkin 1990).

2.2. *Structure functions in the inertial subrange* $\eta \ll r \ll z$

At these scales we expect scaling behaviour to be representative of local isotropy. Following Anselmet *et al.* (1984) the scaling in this inertial subrange can be expressed as

$$\langle \Delta u^n \rangle = C_n(\epsilon r)^{n/3} \left(\frac{r}{\ell}\right)^{\xi_n - n/3}, \tag{2.5}$$

where ξ_n is the anomalous scaling exponent and ℓ is a length scale. The Kolmogorov 1941 theory predicts $\xi_2 = 2/3$ for the second-order structure function as well as $\xi_n = n/3$ for higher-order moments. Data instead show anomalous scaling with $\xi_n < n/3$ for $n > 3$ (Anselmet *et al.* 1984; Sreenivasan & Antonia 1997). The trends can be fitted quite well empirically using the log-Poisson model of She & Leveque (1994),

$$\xi_n = \frac{n}{9} + 2\left[1 - \left(\frac{2}{3}\right)^{n/3}\right], \tag{2.6}$$

or the p-model of Meneveau & Sreenivasan (1987),

$$\xi_n = 1 - \ln_2(0.7^{n/3} + 0.3^{n/3}). \tag{2.7}$$

Thus, for even moments $n = (2, 4, 6, 8, 10)$, we obtain from She & Leveque (1994) $\xi_n = (0.6959, 1.2797, 1.7778, 2.2105, 2.5934)$, and $\xi_n = (0.6937, 1.2822, 1.7859, 2.2289, 2.6321)$ for the p-model, essentially the same within experimental accuracy. For concordance with recent work on even moments, we shall set $n = 2p$ below and only focus on even moments $2p$. Moreover, for wall-bounded flow, using (2.3) and setting $\ell = z$ (the distance to the wall), in non-dimensional form we obtain

$$\langle \Delta u_+^{2p} \rangle^{1/p} = C_{2p}^{1/p}\kappa^{-2/3}\left(\frac{r}{z}\right)^{\xi_{2p}/p} = M_p\left(\frac{r}{z}\right)^{\xi_{2p}/p}, \tag{2.8}$$

with $M_p = C_{2p}^{1/p}\kappa^{-2/3}$. For wall-bounded flows, in the logarithmic layer such scaling is expected to hold in the range $\eta \ll r \ll z$, or $z_+^{-3/4}\kappa^{1/4} \ll r/z \ll 1$.

2.3. *Second-order structure functions at scales* $z < r \ll \delta$

Davidson *et al.* (2006*b*) argued that $\langle \Delta u^2 \rangle$ can be considered as the cumulative energy of eddies of size r and less. They postulated that at scales $r > z$, $\langle \Delta u^2 \rangle$ will be dominated by inertial-scale eddies whose heights are roughly between z and r, with kinetic energy of order U_τ^2. Accordingly, considering $\mathrm{d}\langle \Delta u^2 \rangle/\mathrm{d}r$ as an energy density Davidson *et al.* (2006*b*) proposed that $r\mathrm{d}\langle \Delta u^2 \rangle/\mathrm{d}r$ is a constant proportional to U_τ^2. When integrated, a logarithmic law of the form

$$\langle \Delta u_+^2 \rangle = E_1 + D_1 \ln \frac{r}{z} \tag{2.9}$$

is obtained. The coefficients D_1 and E_1 were evaluated by Davidson *et al.* (2006*b*) based on modelling assumptions and moderate Reynolds number data.

In a more detailed study, Davidson *et al.* (2006*a*) proposed that r should be normalised by the length scale U_τ^3/ϵ rather than z in (2.9). It is worth highlighting that U_τ^3/ϵ is equivalent to scaling with z (after substitution for ϵ using (2.3)), valid at high Reynolds numbers assuming that equilibrium holds. Therefore, they proposed that (2.9) should be replaced by

$$\langle \Delta u_+^2 \rangle = E_1^* - D_1 \ln \frac{\kappa \mathscr{P}}{\epsilon} + D_1 \ln \frac{r}{z}, \tag{2.10}$$

where E_1^* is a constant of order unity. Based on their modelling, Davidson & Krogstad (2009) postulated that E_1^* and D_1 are universal constants in turbulent boundary layers. Indeed, Davidson *et al.* (2006*a*) showed an improvement when using (2.10) (i.e. using U_τ^3/ϵ to normalise r rather than z). This can be attributed to the finite Re range studied. Davidson & Krogstad (2014) further considered these issues for smooth and rough wall flows for structure functions up to sixth order.

We note that for simplicity in the presentation hereafter, the range $z < r \ll \delta$ within the inertial region of structure functions will be referred to as the '$\ln(r/z)$ region', following Davidson and coworkers.

2.4. *Second- and higher-order moments of streamwise velocity*

As summarised in the introduction, there is growing evidence of logarithmic behaviour in the variance of the streamwise velocity fluctuations (Hultmark 2012; Marusic *et al.* 2013), and a similar behaviour in high-order moments has been observed (Meneveau & Marusic 2013). For arbitrary even-order moments, this can be written according to

$$\langle u_+^{2p} \rangle^{1/p} = B_p - A_p \ln \frac{z}{\delta}, \tag{2.11}$$

where for $p = 1$ the scaling of the variance involves the 'Townsend–Perry constant' $A_1 \approx 1.25$. For Gaussian statistics, Meneveau & Marusic (2013) pointed out that $A_p = [(2p-1)!!]^{1/p} A_1$ for higher-order even moments. They found that the values of A_p for $p > 1$ measured from experimental data display sub-Gaussian behaviour, i.e. $A_p < [(2p-1)!!]^{1/p} A_1$. Such results have also been recently obtained in large-eddy simulations by Stevens, Wilczek & Meneveau (2014). Preliminary discussions are also presented for the spanwise and wall-normal velocity components as all velocity components are available from the LES datasets.

It can be noted (Davidson & Krogstad 2009) that (2.11) and (2.9) (evaluated at $r = \delta$) display a dependence on height z that is consistent with the expected limiting behaviour when $r \gg \delta$, $\langle \Delta u_+^2 \rangle = 2\langle u_+^2 \rangle$, with $D_1 = 2A_1$.

2.5. *Postulate for higher-order structure functions at scales $z < r \ll \delta$*

Having considered the points summarised in the preceding sections, we now consider higher-order structure functions in the range $z < r \ll \delta$ (the $\ln(r/z)$ region). If in that range the variance of the velocity increment follows a logarithmic law as in (2.9), then following the same arguments as Meneveau & Marusic (2013) for higher-order moments of velocity fluctuations, one can postulate the following scaling for higher-order structure functions:

$$\langle \Delta u_+^{2p} \rangle^{1/p} = E_p + D_p \ln \frac{r}{z}. \tag{2.12}$$

In particular, when $r = \delta$, one can show (see § 5.1 for more details) that this expression recovers the limiting behaviour consistent with (2.11) for the z dependence

of the logarithmic behaviour of high-order moments at $r \gg \delta$. Further motivation for expecting a logarithmic behaviour of the high-order structure functions can be provided by model calculations based on the attached-eddy hypothesis. As shown in § 5.2, the spatial structure that arises from a superposition of attached eddies can be used to compute velocity increments, and their moments in that range lead directly to logarithmic scaling.

However, first, in the next sections we present empirical evidence for (2.12) based on the experimental data. The analysis of data is presented in § 4.2. Further derivations and the modelling of higher-order structure functions based on the attached-eddy hypothesis are subsequently presented in § 5.

3. The experimental data

The present study utilises five experimental databases, with key parameters provided in table 1. For the present analysis we have chosen databases that have friction Reynolds numbers that exceed $Re_\tau \gtrsim 5000$. This threshold satisfies multiple criteria to consider a boundary layer to be a high Reynolds number flow, which are summarised in a recent review article by Smits *et al.* (2011). These criteria include sufficient scale separation to decouple the viscous and energetic scales (McKeon & Morrison 2007), a constant wake factor (Coles 1962) and over a decade of logarithmic velocity variation in z^+, to name a few. Four datasets were acquired from the High Reynolds Number Boundary Layer Wind Tunnel (HRNBLWT) at the University of Melbourne. This facility has a large working section of 27 m in length, with a cross-sectional area of approximately 2 m $\times$ 1 m. The long working section provides a long development length, leading to a boundary layer thickness of approximately 0.35 m at the end of the working section, and thus presents less acute spatial resolution issues. Further details of the facility are provided in Nickels *et al.* (2005). The two single-wire hot-wire anemometry measurements from this facility are at different streamwise positions and free stream velocities, but are more or less comparable otherwise. Both use 2.5 μm diameter Wollaston wires operated by an in-house constant-temperature anemometer (MUCTA). The spatial resolution in viscous units is shown in table 1 and is considered to be sufficient to resolve the turbulence intensity accurately within the logarithmic region wall-normal locations considered in this study based on the guidelines laid out by Hutchins *et al.* (2009). The other datasets from the Melbourne wind tunnel were obtained from a planar PIV measurement using a unique experimental set-up with multiple cameras to obtain a large field of view (streamwise extent $> 2\delta$) with targeted spatial resolution closer to the wall where it is most critical (de Silva *et al.* 2014). The highly magnified field of view (high-mag FOV) targeted at the near-wall region is ideally suited for this analysis, and provides spatial information across the sublayer and lower region of the logarithmic layer with a spatial resolution of a few viscous length scales. Meanwhile, the large-FOV PIV provides direct spatial information for a large streamwise extent of the order δ.

The final dataset to be considered was acquired using hot-wire anemometry in the surface layer of the atmospheric boundary layer at the Surface Layer Turbulence and Environmental Test Facility (SLTEST) located at the Utah salt flats (Kunkel & Marusic 2006). The measurements involved a vertical array of ten 2.5 μm diameter platinum-coated tungsten wires mounted from $z = 0.005$–2 m (spaced logarithmically in z), The placement of the wires was such that a large proportion of the velocity signals obtained were well within the logarithmic region of the flow. This dataset proved valuable for this work due to the significantly higher Reynolds number of the

Symbol	Facility	Reference	Technique	$\approx Re_\tau$	$\approx \Delta x^+$	$\approx \Delta y^+$	$\approx \Delta z^+$
□	Melbourne	Hutchins *et al.* (2009)	Hot-wire	2 800	—	20	—
◇	Melbourne	Hutchins *et al.* (2009)	Hot-wire	19 000	—	20	—
○	Melbourne	de Silva *et al.* (2014)	High-mag PIV	19 000	15	30	15
●	Melbourne	de Silva *et al.* (2014)	Large-FOV PIV	14 500	40	30	40
△	SLTEST	Kunkel & Marusic (2006)	Hot-wire	3×10^6	—	15	—

TABLE 1. Summary of experiments.

atmospheric boundary layer compared with laboratory experiments. Further details on all measurements can be found in their respective publications.

For consistency, the friction velocity for the dataset from Hutchins *et al.* (2009) was recomputed using the composite velocity profile of Chauhan, Monkewitz & Nagib (2009) with constants $\kappa = 0.384$ and $A = 4.17$. Similarly, the same constants were used for the atmospheric boundary layer dataset of Kunkel & Marusic (2006). However, since velocity signals are only available within the logarithmic region for this dataset, a simple modified Clauser chart fit was employed using the same log-law constants rather than a composite velocity profile.

For the PIV measurement typically the interrogation window size dictates the spatial resolution. However, PIV is usually impacted by experimental noise to a higher degree than its hot-wire counterpart. The influence of noise on turbulence intensity statistics has been studied previously by drawing comparisons between PIV datasets and hot-wire/DNS datasets to determine the noise floor for PIV measurements (Atkinson *et al.* 2013). Following a similar approach, we selected the smallest separation r to compute structure functions such that it was above the noise floor for each PIV measurement. Here the cutoff was chosen based on a direct comparison with a hot-wire dataset at a comparable Reynolds number.

As a final note, prior to proceeding with computing the higher-order moments of the streamwise structure function, the degree of convergence at higher moments needs to be considered. To assess the degree of convergence following the approach described in Meneveau & Marusic (2013) the pre-multiplied probability density function for velocity fluctuations $\Delta u_+^{2p} P(\Delta u_+)$ was computed. The results are shown in figure 1, where (*a*) corresponds to a hot-wire dataset of Hutchins *et al.* (2009) and (*b*) represents the PIV dataset of de Silva *et al.* (2014). For the hot-wire dataset acceptable convergence is observed up to $2p = 10$ in the sense that the area under the curve seems to be captured well with the amount of data available. Conversely, the PIV dataset only shows good convergence up to $2p = 6$, as one may expect due to the significantly lower number of ensembles available ($\approx 6 \times 10^6$ for the hot-wire signal of Hutchins *et al.* 2009 and $\approx 1 \times 10^6$ after considering all captured large-FOV PIV frames of de Silva *et al.* 2014). We note that similar results are obtained for the other datasets employed, where all hot-wire datasets utilised show reasonable convergence up to $2p = 10$ and the high-mag FOV PIV shows a similar degree of convergence to the large-FOV PIV up to $2p = 6$. Therefore, for the subsequent analysis results from the PIV datasets at $2p > 6$ should be considered with due caution.

4. Experimental results

In this section we present results for the structure function of the streamwise velocity across all datasets considered. Here, we place emphasis mainly on the ranges

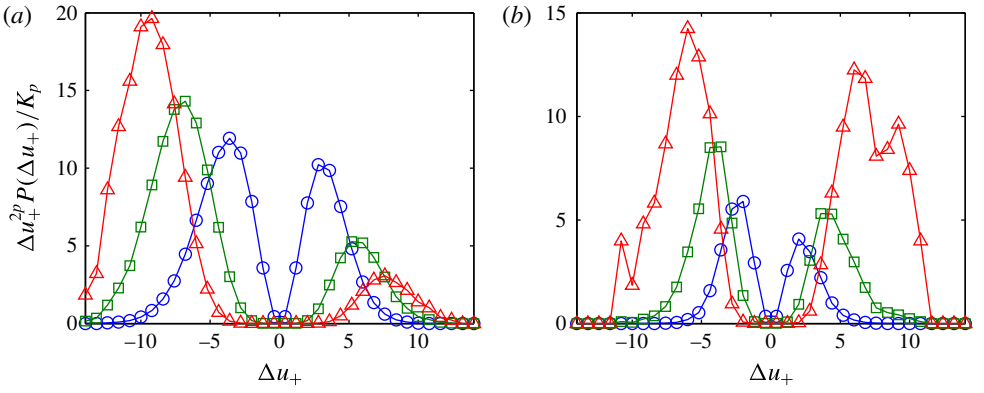

FIGURE 1. (Colour online) Premultiplied probability density function of Δu at $r \approx z^+$, where $z^+ \approx 800$. Both measurements were made in the HRNBLWT. (*a*) Hot-wire data of Hutchins *et al.* (2009), (*b*) large-FOV PIV of de Silva *et al.* (2014). The moments $2p = 2$, 6 and 10 are represented by ○, □ and △ respectively. The curves are separated by an arbitrary factor K_p for clarity.

$\eta \ll r \ll z$ and $z < r \ll \delta$ to investigate the appropriate scaling behaviour. It is noted that the high-mag PIV from the HRNBLWT facility has adequate spatial resolution and streamwise extent to accommodate the inertial subrange ($\eta \ll r \ll z$), but does not provide sufficient spatial information for the $\ln(r/z)$ range ($z < r \ll \delta$). However, the high-mag and large-FOV PIV datasets have been measured simultaneously, and thus the large-FOV PIV dataset, with a spatial extent of the order of δ (de Silva *et al.* 2014), provides the results in the range $z < r \ll \delta$. The PIV data also provide direct spatial information without the need to invoke Taylor's hypothesis, as required for the hot-wire datasets. When Taylor's hypothesis is used in this paper, the convection velocity is taken to be the local mean velocity.

4.1. *Scaling of the second-order structure function and influence of the wall-normal location*

It is valuable to consider how the second-order structure function varies with both the wall-normal position and the spatial separation, and an attempt to illustrate this is shown in figure 2. Here, a three-dimensional view of $\langle \Delta u_+^2 \rangle$ is presented at all measurement locations across the boundary layer height for the hot-wire dataset from Hutchins *et al.* (2009) at $Re_\tau = 19\,000$ with 50 wall-normal locations. The region highlighted in green on the surface formed from these profiles denotes the inertial scaling region where a $\ln(r/z)$ law is observed. Further, the presented three-dimensional surface provides a visual representation of the relationship between the linear–log region observed in $2\langle u_+^2 \rangle$ (● symbols) and the $\ln(r/z)$ law in $\langle \Delta u_+^2 \rangle$ with the same multiplicative constant A_1 (for $p = 1$; (2.11)).

In the following we will focus primarily on data from within the logarithmic region, which we take to be nominally within the range $3\sqrt{Re_\tau} \lesssim z^+ \lesssim 0.15Re_\tau$ following recent observations using high Reynolds number datasets (Klewicki, Fife & Wei 2009; Marusic *et al.* 2013; Chin *et al.* 2014). The two thicker, dark grey lines (red online) shown in figure 2 demarcate this region. The results in figure 2 indicate good support for (2.9), where z is used as the normalising length scale. It is worthwhile to consider whether the refined formulation (2.10) of Davidson *et al.* (2006*a*) is required

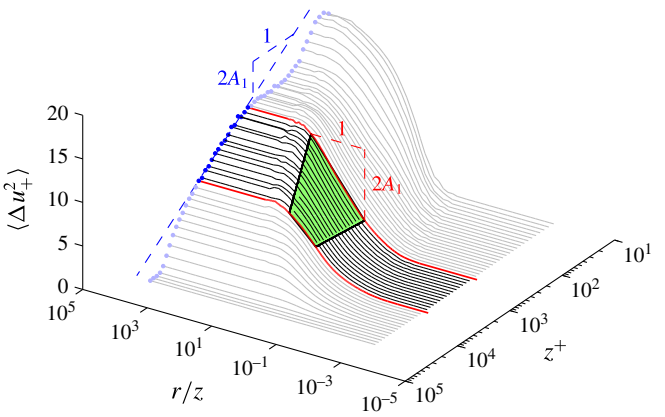

FIGURE 2. (Colour online) Three-dimensional surface generated using profiles of $\langle \Delta u_+^2 \rangle$ versus r/z at all wall-normal locations from the hot-wire dataset of Hutchins *et al.* (2009) at $Re_\tau \approx 19\,000$. The ● symbols correspond to $2\overline{u^2}$ at each wall-normal location. The green shaded region corresponds to where a $\ln(r/z)$ law is expected at wall-normal locations within the logarithmic region, highlighted by the darker contours. The indicated slopes are detailed further in § 6.

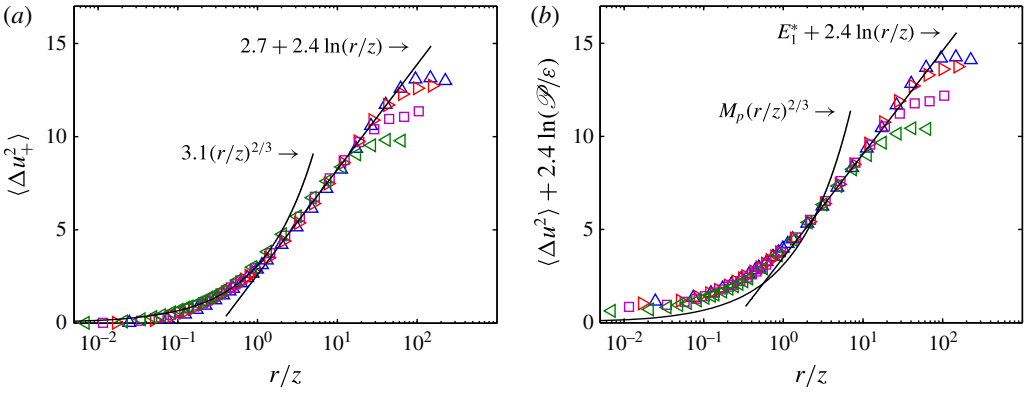

FIGURE 3. (Colour online) (*a*) A plot of $\langle \Delta u_+^2 \rangle$ versus r/z from hot-wire data at $Re_\tau = 19\,000$ of Hutchins *et al.* (2009). Wall-normal locations: △, $z^+ \approx 400$; ▷, 700; □, 1000; ◁, 1900. The locations are selected to be within the logarithmic region. (*b*) A plot of $\langle \Delta u_+^2 \rangle$ versus r/z after applying the correction outlined in (2.10) following Davidson *et al.* (2006*a*). The solid lines correspond to formulations based on (2.9) and (2.10) in (*a*) and (*b*) respectively.

at higher Reynolds numbers. Figure 3 shows a comparison between formulations (2.9) and (2.10) for results within the logarithmic region for the same data as in figure 2. The results show that inclusion of the extra term involving production and dissipation slightly improves the collapse of the data in the inertial range ($z < r \ll \delta$), although its effect is probably not required at this Reynolds number. This is primarily due to the fact that the turbulent production and dissipation rates are nominally equal in the logarithmic region at sufficiently high Reynolds numbers (Tennekes & Lumley 1972; Townsend 1976). Moreover, accurate estimation of the turbulent production

$\approx z^+$	$15\nu\overline{(\partial u/\partial x)^2}$	$15\nu\int_0^\infty k_1^2\phi_{11}(k_1)\mathrm{d}k_1$	Third-order structure function
300	0.53×10^{-2}	0.57×10^{-2}	0.58×10^{-2}
400	0.41×10^{-2}	0.44×10^{-2}	0.47×10^{-2}
500	0.33×10^{-2}	0.34×10^{-2}	0.37×10^{-2}
800	0.23×10^{-2}	0.24×10^{-2}	0.25×10^{-2}
1600	0.12×10^{-2}	0.13×10^{-2}	0.12×10^{-2}

TABLE 2. Dissipation rates ϵ (given in $\mathrm{m}^2\ \mathrm{s}^{-3}$) computed from the hot-wire dataset of Hutchins *et al.* (2009) at $Re_\tau \approx 19\,000$, using three different methods.

and dissipation rates is a challenge experimentally. Here, we estimate production using $\mathscr{P} \approx 1/\kappa z^+$, while for the dissipation rate several estimates can be employed and are summarised in table 2 for the hot-wire dataset at $Re_\tau \approx 19\,000$ (Hutchins *et al.* 2009). All the estimates use the assumption of isotropy (see Pope (2000) for a detailed comparison); however, the third method (column 3) based on the third-order structure function has been reported to have less ambiguity (Sreenivasan & Antonia 1997). The estimates of ϵ show an uncertainty of $\approx\pm20\,\%$ between the methods used, comparable with prior observations by Kunkel & Marusic (2006) and others. It is also worth highlighting that recent work particularly using numerical databases (where one can accurately compute $\mathscr{P}$ and ϵ) has aimed to answer the validity of the balance between $\mathscr{P}$ and ϵ in the inertial region of wall turbulence (Hoyas & Jiménez 2006; Bernardini *et al.* 2014; Lee & Moser 2015, and others). The results have largely shown support for the validity of an approximate balance, thus matching prior experimental observations.

In figure 4 we consider data in the logarithmic region across the other datasets at varying Reynolds numbers. Results are presented on both log–log and log–linear scales to highlight the scaling described previously in § 2. For the inertial subrange shown in figure 4(*a*) evidence of a power-law scaling given by (2.8) is prevalent in all datasets with a scaling exponent close to 2/3. Similarly, a power-law scaling given by (2.4) is observed at the smallest scales within the dissipative range with a scaling exponent of 2. Further, a $\ln(r/z)$ law in the form given by (2.9) is observed at scales larger than the inertial subrange in figure 4(*b*). All scaling regimes are indicated by the solid lines, together with their corresponding coefficients. The low Reynolds number dataset (□ symbols) is included to demonstrate a clear trend with changing Reynolds number, and it emphasises the importance of higher Reynolds number data ($Re_\tau = O(10^4$–$10^5)$) to obtain a sufficiently large scale separation and thus observe all scaling behaviours simultaneously. In future efforts, it will also be valuable to consider whether the scaling behaviour reported extends to the transverse structure function, which has been examined previously by Kurien *et al.* (2000), Jacob *et al.* (2004) and others. As a final note, certain studies have reported power-law behaviour for structure functions (Benzi *et al.* 1999; Toschi *et al.* 1999; Jacob *et al.* 2004, and others), albeit with particular focus on the smaller scales. Our analysis shows clear evidence of a power law in the range $\eta \ll r \ll z$ and a $\ln(r/z)$ law in the range $z < r \ll \delta$. Some of these differences in interpretation may be attributed to the substantially higher Reynolds numbers examined in this study compared with prior work. This provides a large scale separation (large logarithmic region) enabling us to better discern any scaling behaviour. Moreover, a large proportion of studies that reported power-law behaviour alone employed decompositions primarily due to the

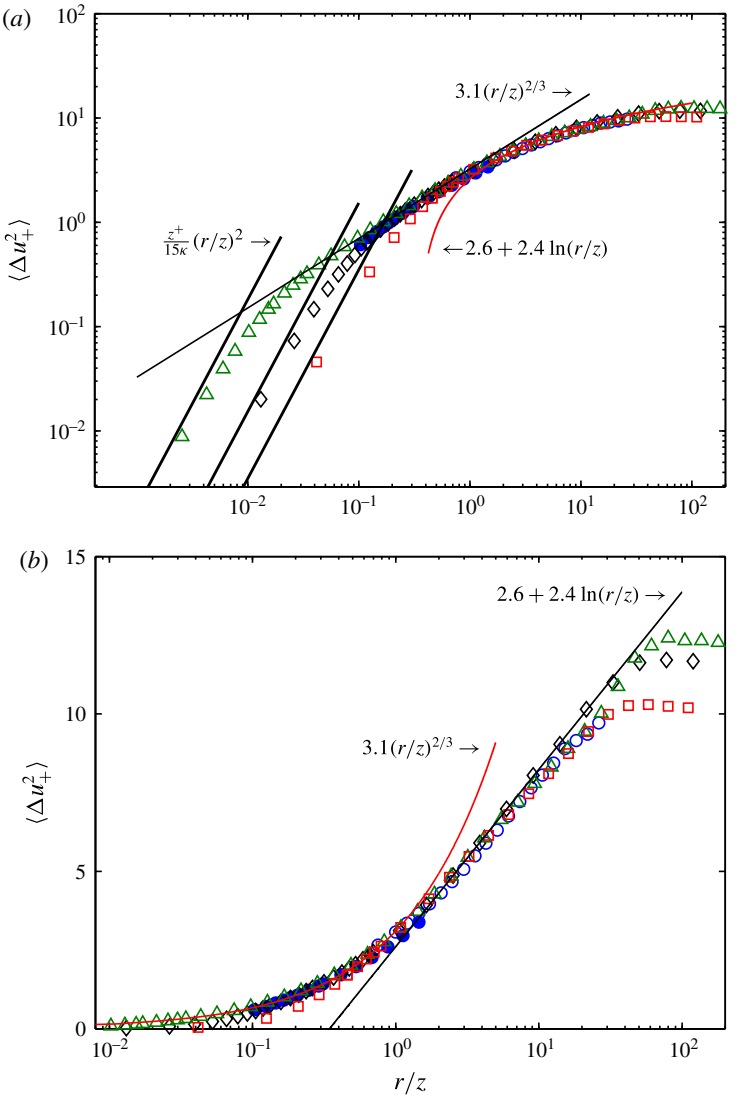

FIGURE 4. (Colour online) Plots of $\langle \Delta u_+^2 \rangle$ versus r/z on (*a*) log–log and (*b*) linear–log scales. The symbols represent different datasets and are defined in table 1. Wall-normal locations: □, $z^+ \approx 200$; ◇, $z^+ \approx 800$; △, $z^+ \approx 1.6 \times 10^4$; ○, ●, $z^+ \approx 800$. The solid lines correspond to fits (detailed further in § 6) in the ranges $\eta \ll r \ll z$ and $z < r \ll \delta$. The heavy solid lines in (*a*) at the smallest r/z represent fits to each hot-wire dataset in the dissipative range.

lack of any scaling behaviour for the structure function in its classical form at the Reynolds numbers considered. Here, we present the structure function in its classical form, where the reported scaling behaviour is clearly observed.

The good agreement between the PIV (denoted by ○, ● symbols) and hot-wire results in figure 4 highlights that the use of Taylor's frozen turbulence hypothesis to convert the time-series information from the hot wires to spatial information is justified for the data presented here, at least up to $r < \delta$. This concurs with previous

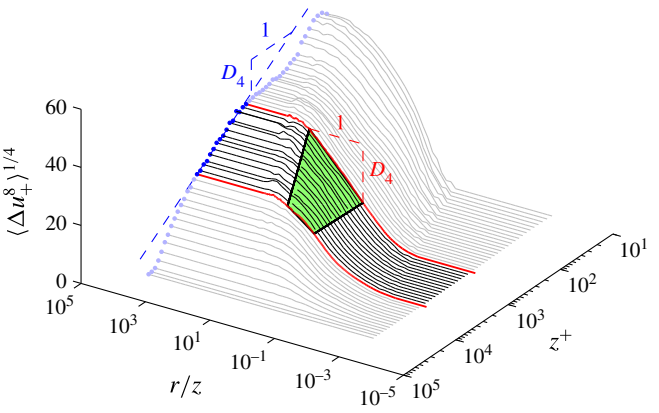

FIGURE 5. (Colour online) Three-dimensional surface generated using profiles of $\langle \Delta u_+^8 \rangle^{1/4}$ versus r/z from the same dataset as presented in figure 2. The symbols are defined in figure 2. The indicated slopes are detailed further in § 6.

findings where other statistical information is compared when Taylor's approximation is invoked, such as in the study of Dennis & Nickels (2008). Other studies that have assessed the accuracy of invoking Taylor's hypothesis include Del Alamo & Jiménez (2009), Chung & McKeon (2010) and Atkinson, Buchmann & Soria (2014).

4.2. *Higher-order structure functions*

Previously, we described the analogous postulate for higher-order structure functions in (2.12), extending prior work by Meneveau & Marusic (2013) for higher-order moments of velocity fluctuations. This section considers empirical evidence for (2.12) based on the experimental data.

To begin, we apply the format used in figure 2 for the eighth-order structure function, which is shown in figure 5. It is immediately evident from figure 5 that the behaviour of the eighth-order structure function (after taking the 1/4 root) is qualitatively comparable with its second-order counterpart. The region highlighted in green on the surface denotes the region where a $\ln(r/z)$ law seems to be prevalent, thus providing empirical support for (2.12). To further validate this observation, figure 6 presents results for the even higher-order moments at a single wall-normal location within the logarithmic region across all the experimental datasets considered, here shown up to $2p = 10$. To accentuate the analogous scaling behaviour observed in the second-order structure function (see figure 4), the solid lines from $2p = 4$–10 in figure 6 represent power- and log-law fits to the HRNBLWT hot-wire dataset. The corresponding coefficients are also indicated in the figure. The universality of these coefficients for the datasets considered will be explored in § 6. The low Re dataset at higher moments shows a deviation from the high Re datasets. This can be attributed to a much smaller logarithmic layer at low Re. Similar Re dependence was also observed by Meneveau & Marusic (2013) for higher-order moments of the streamwise velocity fluctuations below $Re_\tau < 7000$. Our results from structure

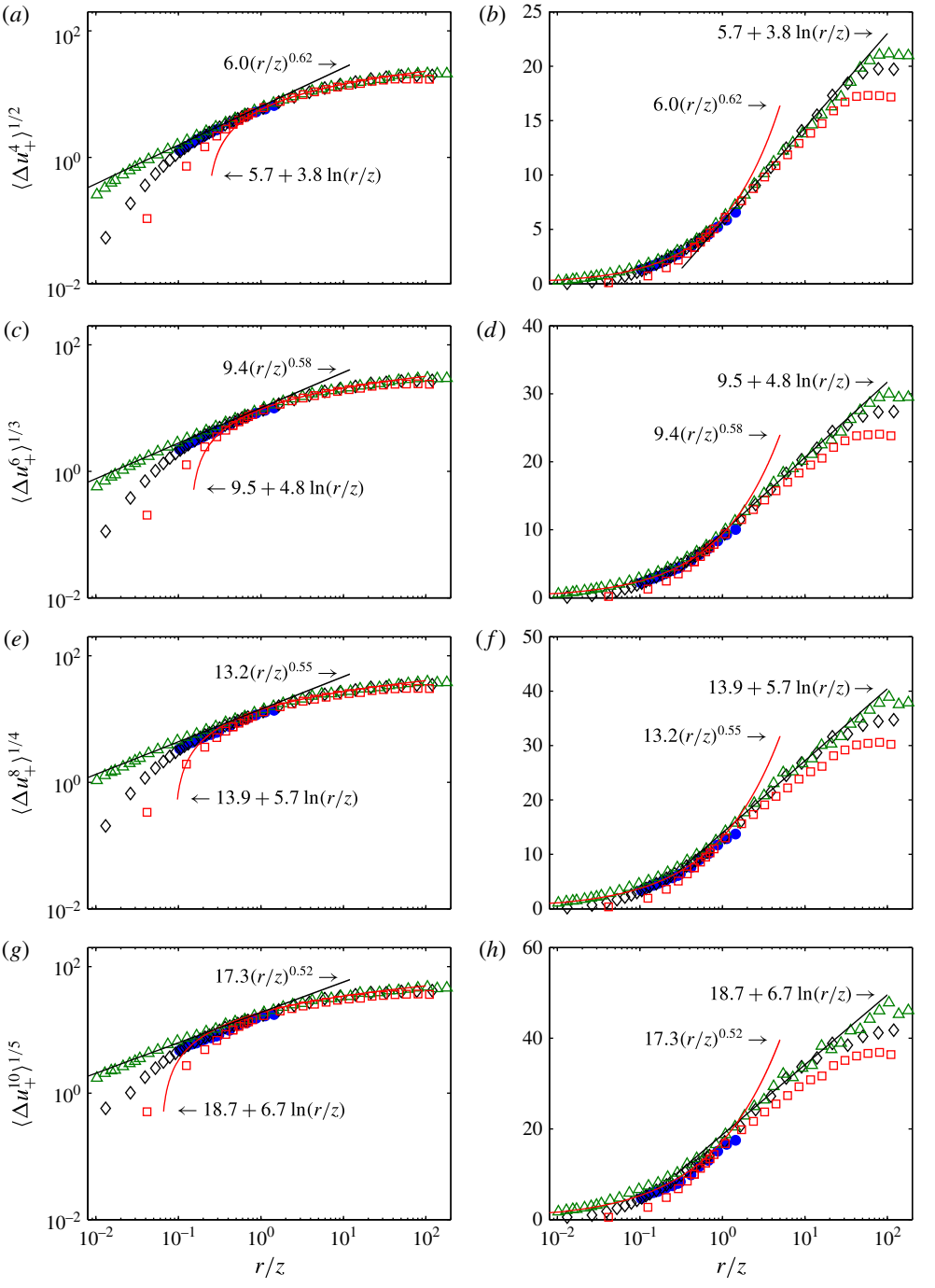

FIGURE 6. (Colour online) Higher-order even structure functions for the same datasets as presented in figure 4: (*a*,*b*) $2p = 4$; (*c*,*d*) $2p = 6$; (*e*,*f*) $2p = 8$; (*g*,*h*) $2p = 10$. The symbols, solid lines and wall positions are defined in table 1 and figure 4 respectively.

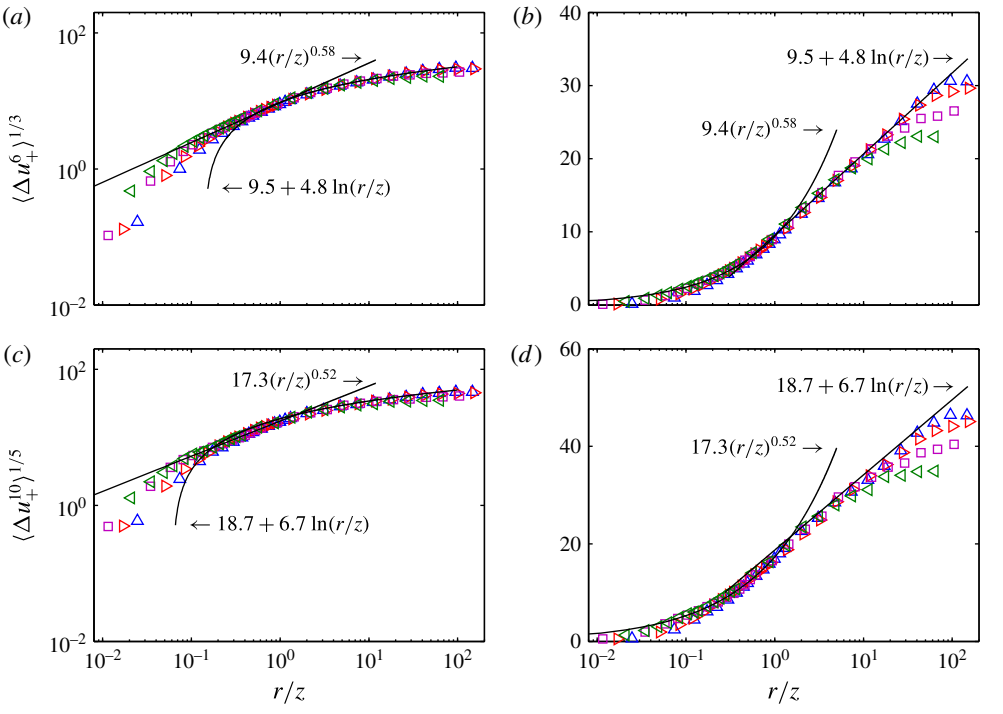

FIGURE 7. (Colour online) Higher-order even structure functions for the same data as presented in figure 3 for various wall-normal positions throughout the logarithmic region for $Re_\tau = 19\,000$: (*a*,*b*) $2p = 6$; (*c*,*d*) $2p = 10$. The symbols, solid lines and wall positions are defined in table 1 and figure 3 respectively.

functions of higher orders are consistent with these findings; that is, beyond this threshold, the higher-order moments are independent of Re. Therefore, we omit the low Re dataset in the subsequent analyses, particularly when computing the coefficients associated with the scaling fits described in § 5.

Figure 7 shows the higher-order results for the data shown in figure 3(*a*) for various wall-normal positions throughout the logarithmic region. The results show good collapse of the higher moments up to $2p = 10$ and provide further direct support for (2.12) across the entire extent of the logarithmic region.

5. Statistical and attached-eddy interpretations in the $\ln(r/z)$ range

In light of the supportive empirical results from the experimental data in § 4.2 for all even higher-order moments based on (2.12), we now aim to bridge the relations previously postulated for the higher-order structure functions with high-order moments of velocity fluctuations. We note that the analysis to follow applies to the inertial range of structure functions within the bounds $z < r \ll \delta$. Two approaches are described in this work. First, we propose a generalisation of the work of Meneveau & Marusic (2013) to higher-order structure functions. We subsequently complement the findings that arise from this generalisation with a physical model of a turbulent boundary layer based on the attached-eddy hypothesis.

5.1. *Relations between high-order moments of velocity fluctuations and structure functions*

Previously, § 2.4 summarised the results from Meneveau & Marusic (2013) for the general behaviour of higher-order velocity fluctuations. Following their work, it is fruitful to develop the limit of structure functions at $r \gg \delta$, by making use of the binomial theorem:

$$\langle \Delta u_+^{2p} \rangle = \sum_{k=0}^{2p} \binom{2p}{k} (-1)^k \langle u_+(x+r)^{2p-k} u_+(x)^k \rangle. \tag{5.1}$$

When $r \gg \delta$, we expect $u_+(x+r)$ and $u_+(x)$ to become statistically independent, and hence $\langle u_+(x+r)^a u_+(x)^b \rangle = \langle u_+(x)^a \rangle \langle u_+(x)^b \rangle$. Therefore,

$$\langle \Delta u_+^{2p} \rangle \to \sum_{k=0}^{2p} \binom{2p}{k} (-1)^k \langle u_+^{2p-k} \rangle \langle u_+^k \rangle. \tag{5.2}$$

If we assume that the odd moments all vanish, then this is equivalent to only adding the positive even terms:

$$\langle \Delta u_+^{2p} \rangle \to \sum_{k=0}^{p} \frac{(2p)!}{(2k)!(2p-2k)!} \langle u_+^{2p-2k} \rangle \langle u_+^{2k} \rangle. \tag{5.3}$$

For $p = 1$, this becomes the familiar $\langle [u_+(\boldsymbol{x}+\boldsymbol{i}r) - u_+(\boldsymbol{x})]^2 \rangle \to 2\langle u_+^2 \rangle$. For $p = 2$, the relationship is $\langle [u_+(\boldsymbol{x}+\boldsymbol{i}r) - u_+(\boldsymbol{x})]^4 \rangle \to 2\langle u_+^4 \rangle + 6\langle u_+^2 \rangle^2$. Using this in the context of the generalised logarithmic laws, for even moments only, we expect

$$\langle \Delta u_+^{2p} \rangle \to \sum_{k=0}^{p} \binom{2p}{2k} \left(B_{p-k} - A_{p-k} \ln(z/\delta)\right)^{p-k} \left(B_k - A_k \ln(z/\delta)\right)^k. \tag{5.4}$$

To simplify, it is useful to absorb the coefficient B_k inside the logarithm, by setting $c_k = \exp(B_k/A_k)$, then we obtain

$$\langle \Delta u_+^{2p} \rangle \to \sum_{k=0}^{p} \frac{(2p)!}{(2k)!(2p-2k)!} \left[A_{p-k} \ln(c_{p-k}\delta/z)\right]^{p-k} \left[A_k \ln(c_k\delta/z)\right]^k. \tag{5.5}$$

Next, we make the reasonable assumption that B_p (as well as c_p) does not depend much on the moment order (e.g. that the intercepts of all moment log-laws occur roughly at the same outer length scale $c_p\delta \approx c\delta$, and based on the measurements of $B_1 \approx 1.7$ and $A_1 \approx 1.25$ we may estimate $c \approx 4$); this seems to be supported by the data. We can then write

$$\langle \Delta u_+^{2p} \rangle \to \left[\ln(c\delta/z)\right]^p \sum_{k=0}^{p} \frac{(2p)!}{(2k)!(2p-2k)!} A_{p-k}^{p-k} A_k^k, \tag{5.6}$$

and we obtain a logarithmic dependence of the structure function asymptote at $r \gg \delta$:

$$\langle \Delta u_+^{2p} \rangle^{1/p} \to G_p \ln\left(\frac{c\delta}{z}\right), \tag{5.7}$$

where

$$G_p = \left(\sum_{k=0}^{p} \frac{(2p)!}{(2k)!(2p-2k)!} A_{p-k}^{p-k} A_k^k \right)^{1/p}. \tag{5.8}$$

Given numeric values for A_p for $p = 1$–5 measured in Meneveau & Marusic (2013), numerical values for G_p can be obtained. For instance, for second-order structure functions, $p = 1$, we obtain

$$G_1 = 2A_1 \approx 2 \times 1.25 \approx 2.5 \tag{5.9}$$

and for fourth-order ones, $p = 2$, we have

$$G_2 = [2(A_2^2 + 3A_1^2)]^{1/2} \approx [2(1.92^2 + 3 \times 1.25^2)]^{1/2} \approx 4.09. \tag{5.10}$$

A comparison of these coefficients against experimental results will be presented in § 6.

5.2. *The attached-eddy hypothesis and higher-order moments*

In this section, we compare the observed statistical behaviour of the structure functions with that predicted by modelling the flow from elementary physical principles. To this end, we derive various properties of the structure functions in the logarithmic region from the attached-eddy hypothesis. This hypothesis states that the logarithmic region is dominated and characterised by the presence of a hierarchy of self-similar coherent structures, or 'eddies', whose sizes scale with their distances from the wall. It is in this loose sense that the eddies are said to be 'attached' to the wall. This will enable us to explore the validity of the current manifestation of the attached-eddy hypothesis as a potential predictive model for structure functions in the logarithmic region of turbulent wall flows.

The attached-eddy hypothesis, as it is applied here, assumes that the locations of the eddies on the wall are perfectly random and independent of each other. This has allowed the statistical properties of the flow to be derived via Campbell's theorem. This model has been used by Woodcock & Marusic (2015) to derive the moments of the velocity in the logarithmic region. The model treats the flow as a superposition of the velocity fields corresponding to each of a multitude of geometrically equivalent eddies. The locations of the eddies are perfectly random and are unaffected by the presence of nearby eddies. (This means that the eddies are not prevented from overlapping, and two or more eddies may occupy the same region of space.) The eddies are identical once scaled by their heights, and their shapes are unaffected by the presence of nearby eddies. The reasoning behind the attached-eddy hypothesis, as well as the derivation extended here, has been further elaborated upon by Woodcock & Marusic (2015).

The height of any particular eddy, h, is assumed to be between h_{min} and h_{max}. We can therefore equate h_{max} with δ, the thickness of the boundary layer. In order to simplify the subsequent equations, we will introduce some new symbols. Since each eddy is characterised by its height, it is sensible to scale all lengths by h. Hence, we scale the location vector, $\boldsymbol{x}$, and the displacement via

$$\boldsymbol{X} \equiv (X, Y, Z) = \frac{\boldsymbol{x}}{h}, \quad R = \frac{r}{h}. \tag{5.11}$$

When deriving the velocity moments, Campbell's theorem reduces the derivation to an integral over the velocity field corresponding to a single eddy. Hence, if the vector $\boldsymbol{Q}(\boldsymbol{X})$ represents the velocity field corresponding to a single eddy, then we can express all moments of the velocity in terms of $\boldsymbol{Q}(\boldsymbol{X})$.

Since each eddy is spatially bounded, the velocity field corresponding to each eddy will inevitably be negligible at a sufficient distance from the location of the eddy, and this distance is proportional to the height of the eddy. Using this, Woodcock & Marusic (2015) showed that the log-law for the flow profile follows from Campbell's theorem.

When applied to the derivation of the structure function, Campbell's theorem reduces the derivation to an integral over a pair of eddies identical in magnitude but of opposite sign, a distance of r apart. We therefore introduce a new function, $\Delta I_k\,(\boldsymbol{X}, R)$, which we call the eddy difference contribution. It relates the flow field corresponding to a single eddy via

$$\Delta I_k(\boldsymbol{X}, R) = \int\!\!\int_{-\infty}^{\infty} \left[Q_x\,(\boldsymbol{X} + \boldsymbol{i}R) - Q_x\,(\boldsymbol{X})\right]^k \mathrm{d}X\mathrm{d}Y. \tag{5.12}$$

This we can relate to $\langle \Delta u_+^n \rangle$ through a mathematical intermediary, which we call a cumulant. These cumulants, denoted by $\Lambda_k(\boldsymbol{x}, r)$, are defined by

$$\Lambda_k(z, r) = \beta \int_{h_{min}}^{h_{max}} \Delta I_k\,(Z, R)\, h^2 P(h)\mathrm{d}h, \tag{5.13}$$

where β denotes the density of the eddies on the wall and $P(h)$ is the probability density function for the height of an eddy. Woodcock & Marusic (2015) have shown that this is given by

$$P(h) = 2\left(h_{min}^{-2} - h_{max}^{-2}\right)^{-1} \frac{1}{h^3}. \tag{5.14}$$

The structure functions can be shown to relate to the cumulants via

$$\langle \Delta u_+^2 \rangle = \Lambda_2, \tag{5.15a}$$

$$\langle \Delta u_+^3 \rangle = \Lambda_3, \tag{5.15b}$$

$$\langle \Delta u_+^4 \rangle = \Lambda_4 + 3\Lambda_2^2, \tag{5.15c}$$

$$\langle \Delta u_+^5 \rangle = \Lambda_5 + 10\Lambda_2\Lambda_3, \tag{5.15d}$$

$$\langle \Delta u_+^6 \rangle = \Lambda_6 + 15\Lambda_2\Lambda_4 + 10\Lambda_3^2 + 15\Lambda_2^3, \tag{5.15e}$$

$$\langle \Delta u_+^7 \rangle = \Lambda_7 + 21\Lambda_2\Lambda_5 + 35\Lambda_3\Lambda_4 + 105\Lambda_2^2\Lambda_3, \tag{5.15f}$$

$$\langle \Delta u_+^8 \rangle = \Lambda_8 + 28\Lambda_2\Lambda_6 + 56\Lambda_3\Lambda_5 + 35\Lambda_4^2 + 210\Lambda_2^2\Lambda_4 + 280\Lambda_2\Lambda_3^2 + 105\Lambda_2^4, \tag{5.15g}$$

$$\langle \Delta u_+^9 \rangle = \Lambda_9 + 36\Lambda_2\Lambda_7 + 84\Lambda_3\Lambda_6 + 126\Lambda_4\Lambda_5 + 378\Lambda_2^2\Lambda_5 + 1260\Lambda_2\Lambda_3\Lambda_4 + 280\Lambda_3^3 + 1260\Lambda_2^3\Lambda_3, \tag{5.15h}$$

$$\langle \Delta u_+^{10} \rangle = \Lambda_{10} + 45\Lambda_2\Lambda_8 + 120\Lambda_3\Lambda_7 + 210\Lambda_4\Lambda_6 + 630\Lambda_2^2\Lambda_6 + 126\Lambda_5^2 + 2520\Lambda_2\Lambda_3\Lambda_5 + 1575\Lambda_2\Lambda_4^2 + 2100\Lambda_3^2\Lambda_4 + 3150\Lambda_2^3\Lambda_4 + 6300\Lambda_2^2\Lambda_3^2 + 945\Lambda_2^5. \tag{5.15i}$$

The derivation of the structure functions is analogous to that presented by Woodcock & Marusic (2015) for the moments of the velocity. The details of this derivation can be found in appendix A. These derivations apply where

$$z \ll r \ll \delta. \tag{5.16}$$

(It should be noted that we have specifically made use of the fact that we equate h_{max} with the height of the boundary layer, δ in the above equation.) In this limit, the even-ordered cumulants will obey

$$\Lambda_k(z, r) = \mathscr{A}_k \log \frac{r}{z} + \mathscr{B}_k, \tag{5.17}$$

where $\mathscr{A}_k$ and $\mathscr{B}_k$ are constants. The constant $\mathscr{A}_k$ is given by

$$\mathscr{A}_k = \frac{4\beta}{h_{min}^{-2} - h_{max}^{-2}} \iint_{-\infty}^{\infty} Q_x^k(X, Y, 0)\mathrm{d}X\mathrm{d}Y. \tag{5.18}$$

(We could give a similar expression for $\mathscr{B}_k$. However, since the attached-eddy model contains different boundary conditions from real turbulent flows, any $\mathscr{B}_k$ derived in this way would not be physically significant.)

We can express the range of eddy sizes present as a Reynolds number. This Reynolds number can be conventionally defined by

$$Re_\tau = 100\frac{h_{max}}{h_{min}}, \tag{5.19}$$

which is based on the assumption that $h_{max} = \delta$ and $h_{min} = 100$ following Kline *et al.* (1967). By an analogous derivation to that given by Woodcock & Marusic (2015), it can be shown that (5.18) can be re-expressed as

$$\mathscr{A}_k = \frac{16}{9}\frac{1}{k_x k_y}\frac{\left(1 - 10^6 Re_\tau^{-3}\right)^2}{\left(1 - 10^4 Re_\tau^{-2}\right)^3} \iint_{-\infty}^{\infty} Q_x^k(X, Y, 0)\mathrm{d}X\mathrm{d}Y, \tag{5.20}$$

where k_x is a constant defined such that the expected distance to the next closest eddy in the positive x direction will always be $k_x h$ if the height of the next closest eddy were known to be h. (More specifically, $k_x h$ represents the distance in a strip of height h' to the nearest eddy of height between h and $h + \mathrm{d}h$ divided by h' and $\mathrm{d}h$.) The constant k_y is its spanwise equivalent.

In the large-Re_τ limit, this asymptotes to

$$\mathscr{A}_k \to \frac{16}{9}\frac{1}{k_x k_y}\left(1 + 3 \times 10^4 Re_\tau^{-2}\right) \iint_{-\infty}^{\infty} Q_x^k(X, Y, 0)\mathrm{d}X\mathrm{d}Y \quad \text{as } Re_\tau \to \infty. \tag{5.21}$$

As we can easily see in (5.15), Λ_2 is equivalent to the second-order structure function. We can therefore return (2.9), the logarithmic law for $\langle \Delta u_+^2 \rangle$, by stating that $\mathscr{A}_2 \equiv D_1$ and $\mathscr{B}_2 \equiv E_1$.

It can also be observed that by considering (5.13) the higher even-ordered structure functions will be dominated by their final term (which is the component containing the highest power of Λ_2) in the limit as $\beta \to \infty$. Given the relationship between Λ_2 and the second-order structure function, we can easily see that (5.17) returns a logarithmic

law for the second-order structure function given in (2.9). Furthermore, for large β ($\beta \to \infty$), it can be seen that the even-numbered higher-ordered structure functions will obey

$$\langle \Delta u_+^{2p} \rangle^{1/p} = D_p \log \frac{r}{z} + E_p, \tag{5.22}$$

where D_p and E_p are constants which are equivalent to $\mathscr{A}_{2p}$ and $\mathscr{B}_{2p}$ respectively. Importantly, this concurs with experimental results, as will be discussed in more detail in § 6. We also note that carrying out the above derivations for the other velocity components shows a similar logarithmic relation for the spanwise velocity, but not for the wall-normal velocity.

The odd-ordered cumulants have also been derived in appendix A. Their behaviour is given in (A 25). They are likely to be of much lower magnitude than their even-ordered counterparts wherever (5.16) applies, so their contributions to the even-ordered structure functions should be negligible. Their contributions to the odd-ordered structure functions are more significant, but since these are of less interest, we do not reproduce them here.

Therefore, we can see that the attached-eddy hypothesis produces predictions for the structure functions in the logarithmic region that are in qualitative agreement with experimental evidence. In order to extend this to a quantitative prediction for the structure functions, it would be necessary to produce a specific function for $\boldsymbol{Q}(\boldsymbol{x})$, the velocity field corresponding to a single eddy. This is, however, beyond the scope of this present work.

6. Evaluation of the universal coefficients

This section revisits the experimental results for the scaling of the streamwise structure function with particular focus on the inertial subrange ($\eta \ll r \ll z$) and the $\ln(r/z)$ range ($z < r \ll \delta$). For the inertial subrange the two coefficients ξ_{2p} and M_p are investigated following the power-law scaling given by (2.8). To do so we compute $\langle \Delta u_+^{2p} \rangle^{1/p} (r/z)^{\xi_{2p}/p}$ and present the results on log–linear plots, as shown in figure 8. From (2.8) a plateau should appear in the inertial subrange. The results in figure 8 do indeed show a plateau, but only convincingly for the very high Reynolds number atmospheric boundary layer data. The wind tunnel data at lower Reynolds number are seen to have a limited inertial subrange as is expected.

The results in figure 8 show that the power-law scaling extends to higher-order moments, at least up to $2p = 10$. The computed coefficients for M_p from the three datasets are shown in figure 9(a) and are listed in table 3. The scaling exponent ξ_{2p}/p has been widely investigated in prior work (She & Leveque 1994; Sreenivasan & Antonia 1997, to name a few). Conventionally, the scaling exponent is presented as ξ_{2p}, and is shown in figure 9(b); for completeness figure 9(c) shows the scaling exponent ξ_{2p}/p. The results show a strong deviation from the Kolmogorov estimate (K41), similar to that observed in several prior numerical and experimental studies, as summarised, for example, by She & Leveque (1994). Nevertheless, the three datasets considered here show good collapse for ξ_{2p} and are also in close proximity to prior results from the She–Leveque model (She & Leveque 1994). Overall the results in figures 8 and 9 support the hypothesis that the constants ξ_{2p} and M_p in (2.8) are universal at high Reynolds numbers. This is based on results from three independent datasets, involving different experimental techniques, facilities and flow conditions (noting that the atmospheric boundary layer is a rough boundary layer).

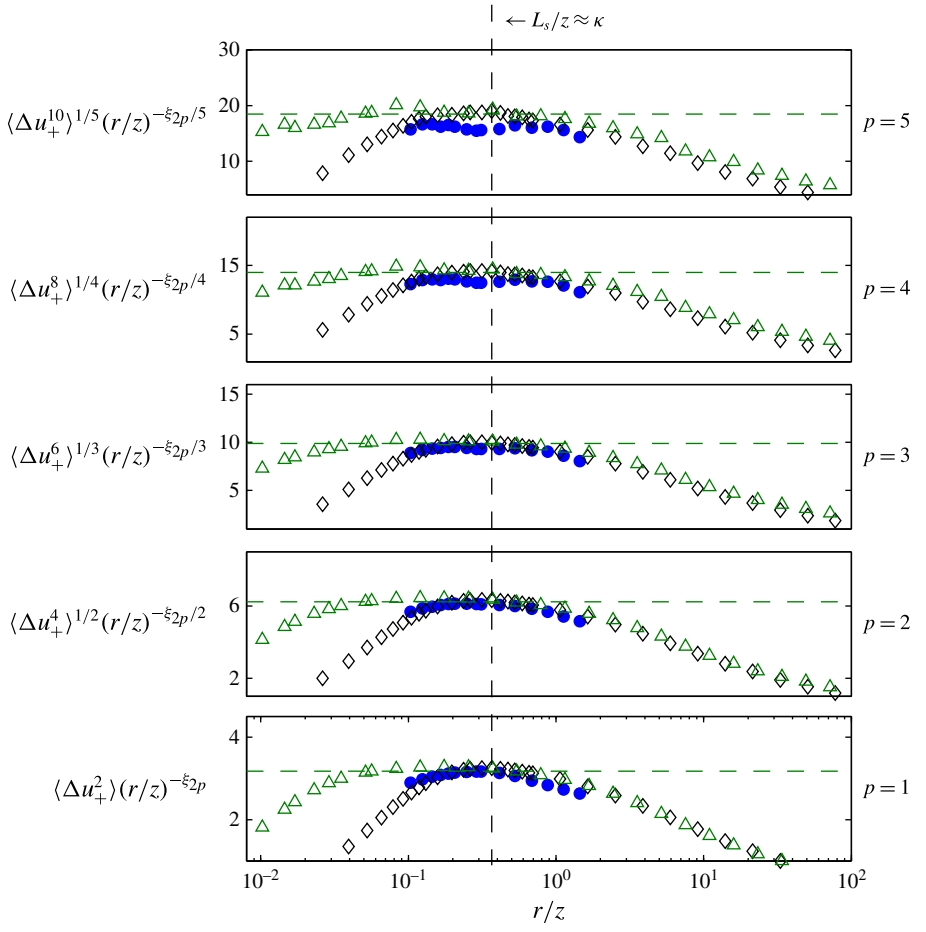

FIGURE 8. (Colour online) Plots of $\langle \Delta u_+^{2p} \rangle^{1/p} (r/z)^{\xi_{2p}/p}$ versus r/z on a linear–log scale at $p = 1$–5. The symbols represent different datasets: ●, HRNBLWT – high-mag PIV; ◇, HRNBLWT – hot-wire; △, SLTEST – hot-wire. Wall-normal locations: ◇, $z^+ \approx 800$; △, $z^+ \approx 1.6 \times 10^4$; ●, $z^+ \approx 800$. The horizontal dashed line indicates the computed multiplicative constant M_p in the inertial subrange $\eta \ll r \ll z$ based on the SLTEST dataset (△ symbols). The vertical dashed line corresponds to the transitional length scale L_s.

For the inertial range within the bounds $z < r \ll \delta$ we expect to observe a $\ln(r/z)$ law in the form given in (5.22) for the higher-order structure functions. Figures 10(*a*) and 10(*b*) show comparisons of D_p and E_p respectively. Also included are the estimates computed using (5.8) with numerical values obtained from Meneveau & Marusic (2013) for A_p. Good agreement is observed between all high Reynolds number datasets considered both visually and quantitatively, as summarised in table 4. We note that the observed variations in the computed coefficients from the higher *Re* datasets are well within the experimental uncertainty of the datasets used. A larger discrepancy is observed between the experimental data and the estimates obtained from (5.8), which can be attributed to the assumptions described in § 5.1.

In figure 8 we also consider the demarcation of the $\ln(r/z)$ range and the inertial subrange using the transitional length scale (L_s) in structure functions, which is

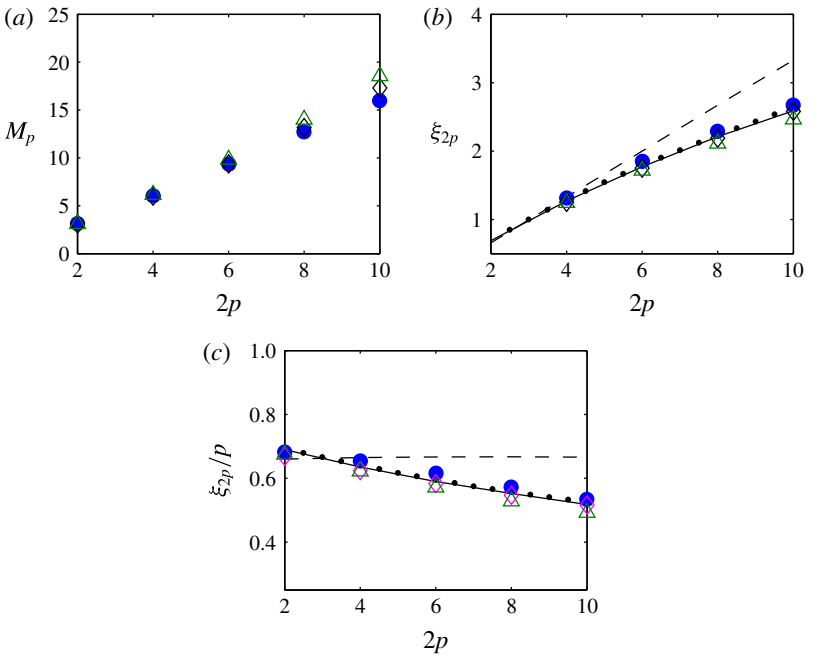

FIGURE 9. (Colour online) (*a*) Multiplicative coefficient (M_p) and (*b*) scaling exponent ξ_{2p}/p of the base r/z for $p = 1$–5 in the inertial sublayer range ($(z^+)^{-3/4} \ll r/z \ll 1$). (*c*) Results in (*a*) reproduced but now scaled with p. The symbols are defined in table 1. The dashed line in (*b*) and (*c*) represents the K41 law, and the solid and dotted lines correspond to numeric values provided in She & Leveque (1994) (see (2.6)) and Meneveau & Sreenivasan (1987) (see (2.7)) respectively.

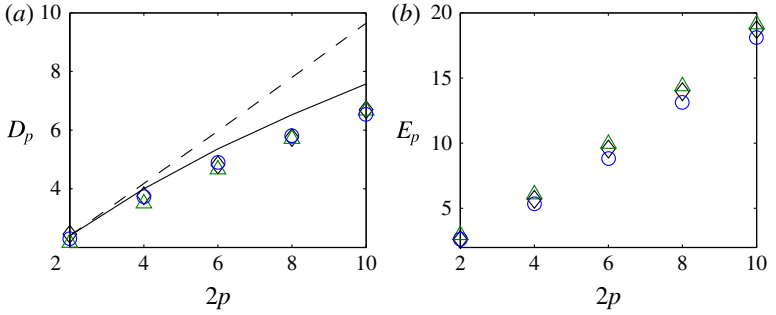

FIGURE 10. (Colour online) (*a*) The multiplicative coefficient (D_p) of r/z at $p = 1$–5 and (*b*) the additive coefficient (E_p) in the scaling range $z < r < \delta$. The symbols are defined in table 1. The dashed line in (*a*) represents the expected behaviour for Gaussian statistics, where $D_p = G_p$ as defined in (5.8), and the solid black line corresponds to numeric values provided in Meneveau & Marusic (2013).

defined as

$$L_s = \sqrt{\epsilon/(\partial\langle U\rangle/\partial z)^3} \tag{6.1}$$

following Toschi *et al.* (1999). Since our analysis is confined to the logarithmic region of wall-bounded turbulence, we can use (2.3) to simplify (6.1) to

$$L_s = \kappa z. \tag{6.2}$$

	SLTEST – hot-wire		HRNBLWT – high-mag PIV		HRNBLWT – hot-wire	
p	ξ_{2p}	M_p	ξ_{2p}	M_p	ξ_{2p}	M_p
1	0.68	3.12	0.68	3.12	0.67	3.11
2	1.24	6.17	1.31	6.06	1.24	6.00
3	1.72	9.84	1.85	9.34	1.75	9.38
4	2.11	14.00	2.29	12.70	2.19	13.16
5	2.46	18.55	2.67	15.94	2.58	17.31

TABLE 3. Comparison of the coefficients ξ_{2p} and M_p in the region $z < r < \delta$ from different datasets. For the HRNBLWT – hot-wire datasets results are presented only at $Re_\tau \approx 19\,000$.

	SLTEST – hot-wire		HRNBLWT – PIV		HRNBLWT – hot-wire		Equation (5.8)
p	D_p	E_p	D_p	E_p	D_p	E_p	$G_p\ (=D_p)$
1	2.16	2.95	2.28	2.62	2.44	2.61	2.50
2	3.50	6.08	3.72	5.33	3.76	5.69	4.09
3	4.66	9.95	4.90	8.81	4.81	9.55	5.42
4	5.70	14.38	5.82	13.10	5.75	13.95	6.55
5	6.67	19.11	6.54	18.11	6.70	18.71	7.60

TABLE 4. Comparison of the coefficients D_p and E_p in the region $z < r < \delta$ from different datasets. Here, G_p is computed using numeric values provided in Meneveau & Marusic (2013) and the estimate $D_p \approx G_p$ (where at $r \approx \delta$ we have $\langle \Delta u_+^{2p} \rangle$ from (5.3)). For the HRNBLWT – hot-wire datasets results are presented only at $Re_\tau \approx 19\,000$.

Similar to prior observations by Saikrishnan *et al.* (2012), albeit at a significantly lower Reynolds number, figure 8 shows that the computed L_s following (6.2) clearly demarcates two distinct scaling regions. At scales below L_s a power-law scaling regime is observed, whereas at scales larger than L_s a less rapidly increasing trend is observed (namely proportional to $\ln(r/z)$, as seen in figures 6 and 7).

6.1. *Modelling of coefficients in the* $\ln(r/z)$ *range*

So far we have examined the inertial subrange and $\ln(r/z)$ range of the streamwise structure function independently. However, the results shown in figures 4 and 6 suggest that the scaling fits employed in each region intersect at approximately $r/z \approx 1$. This suggests the possibility of using this information to reduce the number of unknown constants. (Such matching approaches have been attempted previously, including in the more recent study by Davidson & Krogstad (2009).) Therefore, using this purely empirical observation we equate the two fits and model/estimate the coefficients for the $\ln(r/z)$ range based on the scaling fits in the inertial subrange alone. To perform this, the two scaling fits given by (2.8) and (5.22) are equated to obtain

$$M_p \mathscr{X}^{\xi_{2p}} = E_p' + D_p' \ln \mathscr{X}, \tag{6.3}$$

where E_p' and D_p' are modelled equivalents of E_p and D_p, and $\mathscr{X}$ corresponds to the magnitude of r/z at the estimated point of intersection between the two scaling fits. By further matching gradients at $\mathscr{X}$ we obtain

$$M_p \xi_{2p} \mathscr{X}^{\xi_{2p}-1} = \frac{D_p'}{\mathscr{X}}, \tag{6.4}$$

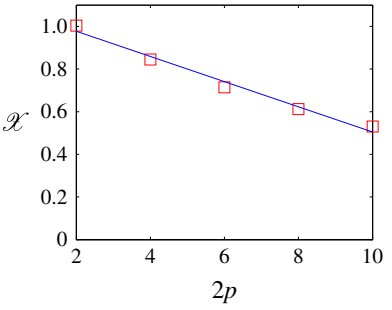

FIGURE 11. (Colour online) Variation of $\mathscr{X}$ computed from the SLTEST dataset of Kunkel & Marusic (2006) at $Re_\tau = 3.1 \times 10^6$ and $z^+ \approx 1.6 \times 10^4$. The solid line represents a linear fit which is used to obtain the results shown in figure 12.

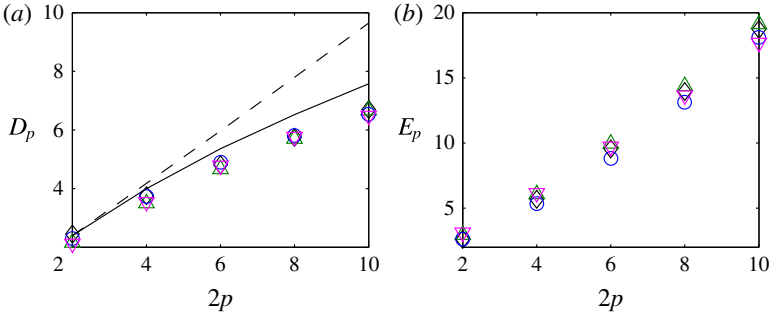

FIGURE 12. (Colour online) The same as figure 10, but with the inclusion of the modelled coefficients ($\triangledown$ symbols) for the SLTEST dataset of Kunkel & Marusic (2006), as summarised in table 5.

which can be rearranged to give

$$D'_p = M_p \xi_{2p} \mathscr{X}^{\xi_{2p}}. \tag{6.5}$$

Substituting (6.5) into (6.3) we can now estimate E'_p using

$$E'_p = M_p \ln \mathscr{X}^{\xi_{2p}} - M_p \xi_{2p} \mathscr{X}^{\xi_{2p}} \ln \mathscr{X} \to M_p \mathscr{X}^{\xi_{2p}} (1 - \xi_{2p} \ln \mathscr{X}). \tag{6.6}$$

Visual inspection of the results presented for $\langle \Delta u_+^{2p} \rangle^{1/p}$ in figures 4 and 6 shows that $\mathscr{X} \approx 1$; however, upon closer inspection a linear decrease in $\mathscr{X}$ is observed across all datasets, as shown in figure 11, with increasing p. Therefore, following estimates of $\mathscr{X}$ from the experimental datasets, results for E'_p and D'_p are summarised in table 5 and are compared with prior experimental results in figure 12. The results show that the magnitude and trend of the modelled coefficients closely match those computed directly from the experimental datasets.

7. Summary and conclusions

Through the use of a uniquely large range of experimental datasets that span several decades of Reynolds numbers, this study investigates the scaling of higher-order

		SLTEST – hot-wire				HRNBLWT – hot-wire			
p	$\mathscr{X}$	D	D_m	E	E_m	D	D_m	E	E_m
1	1.00	2.16	2.12	2.95	3.23	2.44	2.04	2.61	3.11
2	0.84	3.50	3.54	6.08	6.33	3.76	3.41	5.69	5.98
3	0.71	4.66	4.76	9.95	9.94	4.81	4.59	9.55	9.25
4	0.61	5.70	5.75	14.38	13.90	5.75	5.56	13.95	12.79
5	0.53	6.67	6.52	19.11	18.02	6.70	6.28	18.71	16.46

TABLE 5. Comparison of the coefficients D_p and E_p in the region $z < r < \delta$ from different datasets. For the HRNBLWT – hot-wire datasets results are presented only at $Re_\tau \approx 19\,000$.

streamwise structure functions. We present a description of formulations that characterise the scaling laws for the streamwise structure functions with particular focus on the logarithmic region in wall-normal space, which is characterised by a range of locations away from the wall, and within the Kolmogorov inertial subrange and $\ln(r/z)$ range in streamwise separation space.

The employment of datasets with Reynolds numbers extending to $Re_\tau = O(10^6)$ enables us to observe both scaling laws simultaneously unlike most prior work. Furthermore, our analysis shows comparable results for a wide range of experimental datasets extending from laboratory experiments to the atmospheric boundary layer, thus showing a certain degree of universality for the computed coefficients of the scaling laws.

Following prior mathematical descriptions by Davidson and coworkers for the $\ln(r/z)$ range of the second-order structure function, here we show that these descriptions are consistent with the attached-eddy model, which is formulated for the logarithmic region. Moreover, the attached-eddy model is used to derive the expected relations for all higher-order moments, leading to the prediction that all even moments will follow a logarithmic dependence with r/z of the form

$$\langle \Delta u_+^{2p} \rangle^{1/p} = D_p \ln \frac{r}{z} + E_p, \tag{7.1}$$

and this is strongly supported by the experimental results for $2p = 2$–10.

In the inertial subrange, the experimental data also show strong support for a power-law scaling, where the scaling exponent ξ_{2p} is shown to match well with prior data (Anselmet *et al.* 1984; Sreenivasan & Antonia 1997). Further, estimates for the multiplicative constant M_p are presented up to the 10th moment for structure functions, with good agreement observed across all datasets. The transition length scale L_s, studied extensively for shear flows in prior work, is shown to demarcate regions of the structure function with differing scaling behaviour, where a transition from a power law at scales smaller than L_s to a log-law behaviour at larger scales is observed.

The employment of both spatial and temporal datasets enabled us to compute structure functions with and without invoking Taylor's frozen turbulence hypothesis. Our findings show consistent results, highlighting that Taylor's frozen turbulence hypothesis can be used to compute structure functions from temporal data at least up to $r = O(\delta)$. An empirically based approach to model the scaling coefficients within the $\ln(r/z)$ range based on the inertial subrange constants is also presented. Estimates from this model are shown to match well with results computed directly from experimental datasets.

The analysis presented in this paper highlights the universality of the structure function as a tool to understand the scaling behaviour within the logarithmic region of turbulent boundary layers. The consistency in scaling regimes observed in the structure functions from this study complements the findings of Meneveau & Marusic (2013) on the higher moments of the streamwise velocity fluctuations, and provides further statistical information to test the accuracy of both experimental datasets and simulations beyond tests that are usually considered using lower-order statistics.

Acknowledgements

The authors gratefully acknowledge the financial support of the Australian Research Council. C.M. is grateful to the Australian–American Fulbright Commission Senior Scholar Fellowship program for support during initial stages of this work, and the US National Science Foundation (grants CBET 1133800 and IIA 124382) for subsequent support.

Appendix A. Derivation of the functional forms of the structure functions via the attached-eddy model

In this appendix, we present the derivation of the functional forms of the structure functions that are referenced in § 5.2, where we noted that Campbell's theorem reduces the derivation of the structure function to an integral over two identical eddies that are opposite in sign and separated by a distance R. Which pairs of eddies will make a non-negligible contribution to the flow will depend upon two separate and contradictory concerns. If the eddies are too small (i.e. if Z is too large), their contributions to the velocity field may not extend to z. If, however, the eddies are too large (or R is too small), the velocity fields corresponding to the two eddies will overlap, causing a reduction in the magnitude of $Q_x(\boldsymbol{X} + \boldsymbol{i}R) - Q_x(\boldsymbol{X})$, and thereby any even-ordered structure functions.

The derivation of the structure function is largely analogous to the derivation of the moments of the velocity presented by Woodcock & Marusic (2015). Hence, the derivation of $\langle \Delta u_+^n \rangle$ can be found by making the following substitutions within that work:

$$\langle u^n \rangle \longmapsto \langle \Delta u_+^n \rangle, \tag{A 1a}$$

$$Q_x(\boldsymbol{X}) \longmapsto Q_x(\boldsymbol{X} + \boldsymbol{i}R) - Q_x(\boldsymbol{X}), \tag{A 1b}$$

$$I_{n,0,0}(Z) \longmapsto \Delta I_n(Z, R), \tag{A 1c}$$

$$\lambda_{n,0,0}(z) \longmapsto \Lambda_n(z, r). \tag{A 1d}$$

Woodcock & Marusic (2015) derived the functional forms of the velocity moments based upon which eddies will have a non-negligible effect upon the structure function for a particular distance from the wall, z. The derivation of the functional forms of the structure functions presented here is similarly dependent on which eddies' effects are non-negligible for a particular z and separation, r. Derivation of the structure function in this way is very similar to derivation of the moments of the velocity, with a few extra complexities.

The streamwise velocity corresponding to two such eddies can be seen in figure 13 for eddies of various heights. There it can be seen that if the ratio R is sufficiently large, the velocity fields corresponding to the two eddies are effectively independent. Conversely, if R is sufficiently small, the velocity fields corresponding to the two eddies will overlap, and begin to cancel each other out.

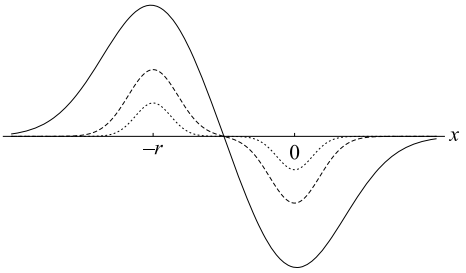

FIGURE 13. Graphical representation of the velocity difference function, $\Delta Q_x(\boldsymbol{X}, R) = Q_x(\boldsymbol{X} + \boldsymbol{i}R) - Q_x(\boldsymbol{X})$, for different eddy heights. (This graph is merely a heuristic guide, and is not intended to represent the exact shape of ΔQ_x.)

Rather than attempt to account for both of these issues simultaneously, we instead deal with them independently. To do so, we first consider the case in which r is sufficiently large that none of the eddies overlap. In this special case the eddy difference contribution defined in (5.12) reduces to

$$\Delta I_k(\boldsymbol{X}, R) = \begin{cases} \displaystyle\iint_{-\infty}^{\infty} 2Q_x^k(\boldsymbol{X})\mathrm{d}X\mathrm{d}Y, & \text{for } k \text{ even}, \\ 0, & \text{for } k \text{ odd}, \end{cases} \qquad \text{for } r \gg h_{max}. \tag{A 2}$$

The value of Λ_{2n} is derived from the above ΔI_{2n} via (5.13). It has previously been shown by Woodcock & Marusic (2015) that so long as $z \ll h_{max}$ a logarithmic dependence upon z will be exhibited. In fact, this can be re-expressed in terms of the function λ_k, which is defined in equation (19) of that article. It is given by

$$\lambda_k(z) = \beta \int_{h_{min}}^{h_{max}} \iint_{-\infty}^{\infty} Q_x^k(\boldsymbol{X})\mathrm{d}X\mathrm{d}Y h^2 P(h)\mathrm{d}h. \tag{A 3}$$

We can account for the effect on ΔI_{2n} of any overlap between $Q_x(\boldsymbol{X} + \boldsymbol{i}R)$ and $Q_x(\boldsymbol{X})$ by including an additional term, $\zeta_k(\boldsymbol{X}, R)$, to account for any overlapping that occurs at low R. The eddy difference contribution becomes

$$\Delta I_k(\boldsymbol{X}, R) = \begin{cases} \displaystyle\iint_{-\infty}^{\infty} 2Q_x^k(\boldsymbol{X})\mathrm{d}X\mathrm{d}Y - \zeta_k, & \text{for } k \text{ even}, \\ -\zeta_k, & \text{for } k \text{ odd}. \end{cases} \tag{A 4}$$

By substituting (A 4) into (5.13), we retrieve

$$\Lambda_k(z, r) = \begin{cases} 2\lambda_k(z) - \beta \displaystyle\int_{h_{min}}^{h_{max}} \zeta_k(\boldsymbol{X}, R) h^2 P(h)\mathrm{d}h, & \text{for } k \text{ even}, \\ -\beta \displaystyle\int_{h_{min}}^{h_{max}} \zeta_k(\boldsymbol{X}, R) h^2 P(h)\mathrm{d}h, & \text{for } k \text{ odd}. \end{cases} \tag{A 5}$$

The value of $\zeta_k(\boldsymbol{X}, R)$ can easily be derived by expanding the brackets in (5.12). For example, we can see that the second-order term is

$$\zeta_2(\boldsymbol{X}, R) = \iint_{-\infty}^{\infty} 2Q_x(\boldsymbol{X})Q_x(\boldsymbol{X} + \boldsymbol{i}R)\mathrm{d}X\mathrm{d}Y. \tag{A 6}$$

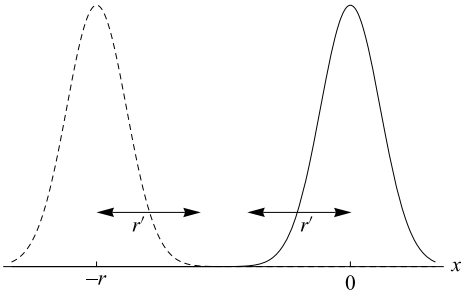

FIGURE 14. Diagram showing $Q_x(\boldsymbol{X})$ and $Q_x(\boldsymbol{X}+\boldsymbol{i}R)$. Here, it can be seen that if Q_x becomes negligible at a distance of r' from the centre of the eddy, then the product $Q_x(\boldsymbol{X})Q_x(\boldsymbol{X}+\boldsymbol{i}R)$ can only be assumed to be universally zero if $r<2r'$.

Higher-order terms will of course contain more components, but what is important is that they will all contain a power of $Q_x(\boldsymbol{X})$ multiplied by a power of $Q_x(\boldsymbol{X}+\boldsymbol{i}R)$. Their exact forms are trivial to determine, but are not necessary for the following derivation.

What is important, however, is that a cursory glance at (5.12) reveals that at $R=0$,

$$\beta\int_{h_{min}}^{h_{max}}\zeta_k\,(\boldsymbol{X},0)\,h^2P(h)\mathrm{d}h=\begin{cases}2\lambda_k(z), & \text{for } k \text{ even},\\ 0, & \text{for } k \text{ odd}.\end{cases} \tag{A 7}$$

The importance of this will be revealed subsequently. The reason for introducing $\zeta_k(\boldsymbol{X},R)$ is that it becomes small when either Z or R is large. We therefore need only exclude eddies that are too small for a given r and z. It is clear that the r dependence of ζ_k is functionally similar to its z dependence in that there will exist a value of r beyond which ζ_k will be negligible, and that this value will be proportional to h. (It is not particularly important what we define to be 'negligible', so long as we are consistent with this definition.) It must be noted, however, that if $Q_x(\boldsymbol{X})$ becomes negligible at $r=r'$, then $Q_x(\boldsymbol{X})Q_x(\boldsymbol{X}+\boldsymbol{i}R)$ will only become negligible at $r=2r'$. This is illustrated in figure 14.

The Biot–Savart law indicates that the velocity field corresponding to a spatially limited vorticity field will diminish as the distance from the vorticity field increases. While the rate at which the velocity field diminishes with distance may depend upon the direction, without knowing the nature of $\boldsymbol{Q}(\boldsymbol{X})$, this is impossible to specify. We do know, however, from the Biot–Savart law that at sufficient distance from the eddy, l,

$$Q_x\left(\frac{l}{h}\right)=O\left(\left(\frac{l}{h}\right)^{-2}\right). \tag{A 8}$$

Importantly, the magnitude of $Q_x(l/h)$ begins to diminish at the same rate regardless of the direction of the displacement. This will allow us to account for r and z simultaneously.

In this case, the equivalent of l would be

$$l=\sqrt{z^2+\frac{r^2}{4}}. \tag{A 9}$$

In this way, we can redefine z and r in a form of polar coordinates. Our angular coordinate, θ, is defined such that

$$r=2l\cos\theta,\quad z=l\sin\theta. \tag{A 10}$$

We can similarly scale this distance with the height of the eddy, so that

$$L = \frac{l}{h} = \frac{1}{h}\sqrt{z^2 + \frac{r^2}{4}}. \tag{A 11}$$

From (A 8), we can see that for sufficiently high l, if we define $\hat{\zeta}_k(L, \theta) \equiv \zeta_k(\boldsymbol{X}, R)$, then

$$\hat{\zeta}_k\,(L, \theta) = \frac{f(\theta)}{L^{2k}}, \tag{A 12}$$

where $f(\theta)$ represents the fact that the velocity field may diminish faster with z than with r. It should be noted that if $r \gg z$, then θ, and hence $f(\theta)$, will change negligibly with r.

Hence, in the $r \gg z$ case, we can simply say that

$$\hat{\zeta}_k\,(L) \propto \frac{1}{L^{2k}}. \tag{A 13}$$

A.1. *Even-ordered cumulants*

We are now able to follow a very similar derivation to that presented by Woodcock & Marusic (2015) in order to derive the even-ordered cumulants, Λ_{2n}. First, we rewrite (A 5) as

$$\Lambda_{2n}(z, r) = 2\lambda_{2n}(z) - \beta \int_{h_{min}}^{h_{max}} \hat{\zeta}_{2n}\,(L)\, h^2 P(h)\mathrm{d}h, \quad \text{for } r \gg z. \tag{A 14}$$

If we assume that there exists a number η such that if $l/h > \eta$, ζ_k will be negligible, we therefore say that

$$\hat{\zeta}_k\,(L) \approx 0, \quad l > \eta h. \tag{A 15}$$

Because $\hat{\zeta}_k$ is assumed to be non-zero only if $l/\eta < h \leqslant h_{max}$, we need not integrate from h_{min} to h_{max} in (5.13). Therefore, (5.13) can be written as

$$\Lambda_{2n}(z, r) = \begin{cases} 2\lambda_{2n}(z) - \beta \displaystyle\int_{l/\eta}^{h_{max}} \hat{\zeta}_{2n}\,(L)\, h^2 P(h)\mathrm{d}h, & \text{for } l > \eta h_{min}, \\ 2\lambda_{2n}(z) - \beta \displaystyle\int_{h_{min}}^{h_{max}} \hat{\zeta}_{2n}\,(L)\, h^2 P(h)\mathrm{d}h, & \text{for } l \leqslant \eta h_{min}. \end{cases} \tag{A 16}$$

If we take the $l > \eta h_{min}$ case in the above equation, and substitute (5.14) for $P(h)$, it can be rewritten as

$$\Lambda_{2n}(z, r) = 2\lambda_{2n}(z) - 2\beta(h_{min}^{-2} - h_{max}^{-2})^{-1} \int_{l/h_{max}}^{\eta} \frac{\hat{\zeta}_{2n}\,(L)}{L}\mathrm{d}L. \tag{A 17}$$

In order to derive the functional form of the structure function from the above equation we first recognise that a major contribution to the integral above will emanate from near $L = 0$. This, coupled with the fact that $\hat{\zeta}_{2n}\,(L)$ will at some point begin to diminish as L increases, indicates that it is reasonable to expand $\hat{\zeta}_{2n}$ in a Taylor series around $L = 0$. This gives

$$\hat{\zeta}_k(L) = \hat{\zeta}_k(0) + L\hat{\zeta}_k'(0) + \frac{L^2}{2!}\hat{\zeta}_k'(0) + \cdots. \tag{A 18}$$

If $l \ll h_{max}$, it is the first term in this expansion that will dominate within the integral. We can therefore say that

$$\Lambda_{2n}(z, r) \simeq 2\lambda_{2n}(z) - 2\beta(h_{min}^{-2} - h_{max}^{-2})^{-1}\hat{\zeta}_{2n}(0) \ln\left(\frac{l}{h_{max}}\right), \quad \text{for } l \ll h_{max}. \tag{A 19}$$

We may further simplify this result by recognising that $\hat{\zeta}_k$ may be related to the eddy contribution function $I_{k,0,0}$, which was defined by Woodcock & Marusic (2015) and is given in equation (18) of that work. From (A 7) of the present paper, we can see that

$$\hat{\zeta}_k(0) = \zeta_k(0, 0) = 2I_{k,0,0}(0). \tag{A 20}$$

By taking into account equation (38) of Woodcock & Marusic (2015), we can see that

$$\Lambda_k(z, r) = \mathscr{A}_k \ln\sqrt{\frac{r^2}{4z^2} + 1} + \mathscr{C}_k, \quad \text{for } k \text{ even}, \tag{A 21a}$$

where $\mathscr{A}_k$ and $\mathscr{C}_k$ are constants, and $\mathscr{A}_k$ is given by

$$\mathscr{A}_k = 4\frac{\beta}{h_{min}^{-2} - h_{max}^{-2}} I_{k,0,0}(0). \tag{A 21b}$$

Because the boundary conditions applied within the attached-eddy model are starkly different from the no-slip boundary conditions that apply to real turbulent flows, we cannot derive a realistic approximation for $\mathscr{C}_k$ via this method. Therefore, although we could derive an equivalent expression to the above for $\mathscr{C}_k$, we elect not to do so.

Of course, since we have already made the important assumption that $r \gg z$, the above expression for $\Lambda_k(z, r)$ can be easily simplified to

$$\Lambda_k(z, r) = \mathscr{A}_k \ln\frac{r}{z} + \mathscr{B}_k, \tag{A 22}$$

where $\mathscr{B}_k$ is a constant. It should be noted that $\mathscr{C}_k$ in (A 21*a*) has been replaced by $\mathscr{B}_k$ in the above equation. This is because the value of the additive constant has been altered. This expression concurs with that given by Davidson *et al.* (2006*b*).

A.2. *Odd-ordered cumulants*

The derivation of the odd-ordered cumulants progresses via an entirely analogous path to their even-ordered counterparts, with the important exception that (A 5) and (A 7) take very different forms.

The important implication of (A 7) is that

$$\hat{\zeta}_k(0) = \zeta_k(0, 0) = 0. \tag{A 23}$$

By proceeding in the same manner as in the even-ordered case, we find that if $l \ll h_{max}$,

$$\Lambda_k(z, r) = 4\frac{\beta}{h_{min}^{-2} - h_{max}^{-2}}\hat{\zeta}_k'(0)\frac{l}{h_{max}} + \mathscr{B}_k, \quad \text{for } k \text{ odd}. \tag{A 24}$$

Using (A 5), this becomes

$$\Lambda_k(z, r) = 4\frac{\beta}{h_{min}^{-2} - h_{max}^{-2}}\frac{z^2 + \frac{r^2}{4}}{h_{max}}\left[\frac{1}{z}\frac{\partial\Delta I_k(0)}{\partial z} + \frac{4}{r}\frac{\partial\Delta I_k(0)}{\partial r}\right] + \mathscr{B}_k, \quad \text{for } k \text{ odd}. \tag{A 25}$$

A comparison with the scaling behaviour derived here for the odd-order structure functions shows results that compare favourably with those measured experimentally. An in-depth presentation and analysis of odd-order moments is relegated to a future communication since this paper is focused on even-order moments.

REFERENCES

ANSELMET, F., GAGNE, YL., HOPFINGER, E. J. & ANTONIA, R. A. 1984 High-order velocity structure functions in turbulent shear flows. *J. Fluid Mech.* **140** (63), 63–89.

ARAD, I., BIFERALE, L., MAZZITELLI, I. & PROCACCIA, I. 1999 Disentangling scaling properties in anisotropic and inhomogeneous turbulence. *Phys. Rev. Lett.* **82** (25), 5040–5043.

ATKINSON, C., BUCHMANN, N. A., AMILI, O. & SORIA, J. 2013 Appropriate spatial filtering of 2D and 3D PIV measurements of wall-bounded turbulent flows. In *PIV 13; 10th International Symposium on Particle Image Velocimetry, Delft, The Netherlands, July 1–3, 2013*, Delft University of Technology, Faculty of Mechanical, Maritime and Materials Engineering, and Faculty of Aerospace Engineering.

ATKINSON, C., BUCHMANN, N. A. & SORIA, J. 2014 An experimental investigation of turbulent convection velocities in a turbulent boundary layer. *Flow Turbul. Combust.* **94**, 1–17.

BENZI, R., AMATI, G., CASCIOLA, C. M., TOSCHI, F. & PIVA, R. 1999 Intermittency and scaling laws for wall bounded turbulence. *Phys. Fluids* **11** (6), 1284–1286.

BERNARDINI, M., PIROZZOLI, S. & ORLANDI, P. 2014 Velocity statistics in turbulent channel flow up to $Re_\tau \approx 4000$. *J. Fluid Mech.* **742**, 171–191.

CASCIOLA, C. M., GUALTIERI, P., BENZI, R. & PIVA, R. 2003 Scale-by-scale budget and similarity laws for shear turbulence. *J. Fluid Mech.* **476**, 105–114.

CASCIOLA, C. M., GUALTIERI, P., JACOB, B. & PIVA, R. 2005 Scaling properties in the production range of shear dominated flows. *Phys. Rev. Lett.* **95** (2), 024503.

CHAUHAN, K. A., MONKEWITZ, P. A. & NAGIB, H. M. 2009 Criteria for assessing experiments in zero pressure gradient boundary layers. *Fluid Dyn. Res.* **41** (2), 021404.

CHIN, C., PHILIP, J., KLEWICKI, J., OOI, A. & MARUSIC, I. 2014 Reynolds-number-dependent turbulent inertia and onset of log region in pipe flows. *J. Fluid Mech.* **757**, 747–769.

CHUNG, D. & MCKEON, B. J. 2010 Large-eddy simulation of large-scale structures in long channel flow. *J. Fluid Mech.* **661**, 341–364.

COLES, D. 1962 The turbulent boundary layer in a compressible fluid, *Tech. Rep.* R-403-PR. The RAND Corporation.

DAVIDSON, P. A. & KROGSTAD, P. Å. 2009 A simple model for the streamwise fluctuations in the log-law region of a boundary layer. *Phys. Fluids* **21** (5), 055105.

DAVIDSON, P. A. & KROGSTAD, P. Å. 2014 A universal scaling for low-order structure functions in the log-law region of smooth- and rough-wall boundary layers. *J. Fluid Mech.* **752**, 140–156.

DAVIDSON, P. A., KROGSTAD, P. A. & NICKELS, T. B. 2006*a* A refined interpretation of the logarithmic structure function law in wall layer turbulence. *Phys. Fluids* **18** (6).

DAVIDSON, P. A., NICKELS, T. B. & KROGSTAD, P.-Å. 2006*b* The logarithmic structure function law in wall-layer turbulence. *J. Fluid Mech.* **550**, 51–60.

DEL ALAMO, J. C. & JIMÉNEZ, J. 2009 Estimation of turbulent convection velocities and corrections to Taylor's approximation. *J. Fluid Mech.* **640**, 5–26.

DENNIS, D. J. C. & NICKELS, T. B. 2008 On the limitations of Taylor's hypothesis in constructing long structures in a turbulent boundary layer. *J. Fluid Mech.* **614**, 197–206.

FRISCH, U. 1995 *Turbulence: the Legacy of AN Kolmogorov*. Cambridge University Press.

GUALTIERI, P., CASCIOLA, C. M., BENZI, R., AMATI, G. & PIVA, R. 2002 Scaling laws and intermittency in homogeneous shear flow. *Phys. Fluids* **14** (2), 583–596.

HINZE, J. O. 1975 *Turbulence*, 2nd edn. McGraw-Hill.

HÖGSTRÖM, U., HUNT, J. C. R. & SMEDMAN, A.-S. 2002 Theory and measurements for turbulence spectra and variances in the atmospheric neutral surface layer. *Boundary-Layer Meteorol.* **103**, 101–124.

HOYAS, S. & JIMÉNEZ, J. 2006 Scaling of the velocity fluctuations in turbulent channels up to $Re_\tau = 2003$. *Phys. Fluids* **18**, 011702.

HULTMARK, M. 2012 A theory for the streamwise turbulent fluctuations in high Reynolds number pipe flow. *J. Fluid Mech.* **707**, 575–584.

HUTCHINS, N., NICKELS, T. B., MARUSIC, I. & CHONG, M. S. 2009 Hot-wire spatial resolution issues in wall-bounded turbulence. *J. Fluid Mech.* **635**, 103–136.

JACOB, B., BIFERALE, L., IUSO, G. & CASCIOLA, C. M. 2004 Anisotropic fluctuations in turbulent shear flows. *Phys. Fluids* **16** (11), 4135–4142.

JIMÉNEZ, J. 2012 Cascades in wall-bounded turbulence. *Annu. Rev. Fluid Mech.* **44**, 27–45.

KLEWICKI, J., FIFE, P. & WEI, T. 2009 On the logarithmic mean profile. *J. Fluid Mech.* **638**, 73–93.

KLINE, S. J., REYNOLDS, W. C., SCHRAUB, F. A. & RUNSTADLER, P. W. 1967 The structure of turbulent boundary layers. *J. Fluid Mech.* **30**, 741–773.

KOLMOGOROV, A. N. 1941 Finite size corrections to scaling in high Reynolds number turbulence. *C. R. Acad. Sci. URSS* **30**, 301–305.

KUNKEL, G. J. & MARUSIC, I. 2006 Study of the near-wall-turbulent region of the high Reynolds number boundary layer using an atmospheric flow. *J. Fluid Mech.* **548**, 375–402.

KURIEN, S., LVOV, V. S., PROCACCIA, I. & SREENIVASAN, K. R. 2000 Scaling structure of the velocity statistics in atmospheric boundary layers. *Phys. Rev.* E **61** (1), 407.

LEE, M. & MOSER, R. D. 2015 Direct numerical simulation of turbulent channel flow up to $Re_\tau = 5200$. *J. Fluid Mech.* (under review), http://arxiv.org/abs/1410.7809.

MARUSIC, I. 2001 On the role of large-scale structures in wall turbulence. *Phys. Fluids* **13**, 735.

MARUSIC, I., MONTY, J. P., HULTMARK, M. & SMITS, A. J. 2013 On the logarithmic region in wall turbulence. *J. Fluid Mech.* **716**, R3.

MCKEON, B. J. & MORRISON, J. F. 2007 Asymptotic scaling in turbulent pipe flow. *Phil. Trans. R. Soc. Lond.* A **365** (1852), 771–787.

MENEVEAU, C. & MARUSIC, I. 2013 Generalized logarithmic law for high-order moments in turbulent boundary layers. *J. Fluid Mech.* **719**, R1–R11.

MENEVEAU, C. & SREENIVASAN, K. R. 1987 Simple multifractal cascade model for fully developed turbulence. *Phys. Rev. Lett.* **59** (13), 1424.

MORRISON, J. F., MCKEON, B. J., JIANG, W. & SMITS, A. J. 2004 Scaling of the streamwise velocity component in turbulent pipe flow. *J. Fluid Mech.* **508**, 99–131.

NELKIN, M. 1990 Multifractal scaling of velocity derivatives in turbulence. *Phys. Rev.* A **42** (12), 7226–7229.

NICKELS, T. B., MARUSIC, I., HAFEZ, S. & CHONG, M. S. 2005 Evidence of the k_1^{-1} law in a high Reynolds number turbulent boundary layer. *Phy. Rev. Lett.* **95** (7), 074501.

PERRY, A. E. & CHONG, M. S. 1982 On the mechanism of wall turbulence. *J. Fluid Mech.* **119** (173), 106–121.

PERRY, A. E., HENBEST, S. M. & CHONG, M. 1986 A theoretical and experimental study of wall turbulence. *J. Fluid Mech.* **165**, 163–199.

PERRY, A. E. & LI, J. DS. 1990 Experimental support for the attached-eddy hypothesis in zero-pressure-gradient turbulent boundary layers. *J. Fluid Mech.* **218**, 405–438.

PERRY, A. E. & MARUSIC, I. 1995 A wall-wake model for the turbulence structure of boundary layers. Part 1. Extension of the attached eddy hypothesis. *J. Fluid Mech.* **298**, 361–388.

PIROZZOLI, S. & BERNARDINI, M. 2013 Probing high-Reynolds-number effects in numerical boundary layers. *Phys. Fluids* **25**, 021704.

POGGI, D., PORPORATO, A. & RIDOLFI, L. 2003 Analysis of the small-scale structure of turbulence on smooth and rough walls. *Phys. Fluids* **15** (1), 35–46.

POPE, S. B. 2000 *Turbulent Flows*. Cambridge University Press.

SAIKRISHNAN, N., DE ANGELIS, E., LONGMIRE, E. K., MARUSIC, I., CASCIOLA, C. M. & PIVA, R. 2012 Reynolds number effects on scale energy balance in wall turbulence. *Phys. Fluids* **24** (1), 015101.

SCHULTZ, M. P. & FLACK, K. A. 2005 Outer layer similarity in fully rough turbulent boundary layers. *Exp. Fluids* **38** (3), 328–340.

SHE, Z. S. & LEVEQUE, E. 1994 Universal scaling law in fully developed turbulence. *Phys. Rev. Lett.* **72**, 1424.

SILLERO, J. A., JIMÉNEZ, J. & MOSER, R. D. 2013 One-point statistics for turbulent wall-bounded flows at Reynolds numbers up to $\delta^+ = 2000$. *Phys. Fluids* **25** (10), 105102.

DE SILVA, C. M., GNANAMANICKAM, E. P., ATKINSON, C., BUCHMANN, N. A., HUTCHINS, N., SORIA, J. & MARUSIC, I. 2014 High spatial range velocity measurements in a high Reynolds number turbulent boundary layer. *Phys. Fluids* **26** (2), 025117.

SMITS, A. J., MCKEON, B. J. & MARUSIC, I. 2011 High-Reynolds number wall turbulence. *Annu. Rev. Fluid Mech.* **43**, 353–375.

SREENIVASAN, K. R. & ANTONIA, R. A. 1997 The phenomenology of small-scale turbulence. *Annu. Rev. Fluid Mech.* **29**, 435–472.

STEVENS, R., WILCZEK, M. & MENEVEAU, C. 2014 Large-eddy simulation study of the logarithmic law for second- and higher-order moments in turbulent wall-bounded flow. *J. Fluid Mech.* **757**, 888–907.

TALLURU, K. M., BAIDYA, R., HUTCHINS, N. & MARUSIC, I. 2014 Amplitude modulation of all three velocity components in turbulent boundary layers. *J. Fluid Mech.* **746**, R1.

TENNEKES, H. & LUMLEY, J. L. 1972 *A First Course in Turbulence*. MIT Press.

TOSCHI, F., AMATI, G., SUCCI, S., BENZI, R. & PIVA, R. 1999 Intermittency and structure functions in channel flow turbulence. *Phys. Rev. Lett.* **82** (25), 5044–5047.

TOWNSEND, A. A. 1976 *The Structure of Turbulent Shear Flow*, 2nd edn. Cambridge University Press.

WOODCOCK, J. D. & MARUSIC, I. 2015 The statistical behaviour of attached eddies. *Phys. Fluids* **27** (1), 015104.

ZHAO, R. & SMITS, A. J. 2007 Scaling of the wall-normal turbulence component in high Reynolds number pipe flow. *J. Fluid Mech.* **576**, 457–473.